scientific reports

Check for updates

OPEN

Emergence of topological superconductivity in doped topological Dirac semimetals under symmetry-lowering lattice distortions

Sangmo Cheon[1,2,3,4,9], Ki Hoon Lee[1,2,5,9], Suk Bum Chung[1,2,6,7]✉ & Bohm-Jung Yang[1,2,8]✉

Recently, unconventional superconductivity having a zero-bias conductance peak is reported in doped topological Dirac semimetal (DSM) with lattice distortion. Motivated by the experiments, we theoretically study the possible symmetry-lowering lattice distortions and their effects on the emergence of unconventional superconductivity in doped topological DSM. We find four types of symmetry-lowering lattice distortions that reproduce the crystal symmetries relevant to experiments from the group-theoretical analysis. Considering inter-orbital and intra-orbital electron density-density interactions, we calculate superconducting phase diagrams. We find that the lattice distortions can induce unconventional superconductivity hosting gapless surface Andreev bound states (SABS). Depending on the lattice distortions and superconducting pairing interactions, the unconventional inversion-odd-parity superconductivity can be either topological nodal superconductivity hosting a flat SABS or topological crystalline superconductivity hosting a gapless SABS. Remarkably, the lattice distortions increase the superconducting critical temperature, which is consistent with the experiments. Our work opens a pathway to explore and control pressure-induced topological superconductivity in doped topological semimetals.

Topological insulator, Dirac semimetal (DSM), Weyl semimetal, and topological superconductor are newly established quantum states of matter which are expected to have applications for dissipationless devices and quantum information technologies[1–7]. Among them, topological Weyl and Dirac semimetals are characterized by relativistic quasi-particles and gapless nodes in bulk spectra[3,6,8–11]. Because of their anomalous electromagnetic responses and topologically-protected surface Fermi arcs on the boundaries, such topological semimetals have been attracted much attention[6,8,12–26]. Moreover, due to the unique properties of Dirac and Weyl semimetals, extensive theoretical and experimental studies of their superconducting instabilities have been conducted to observe possible topological superconductivity[5,7].

Recently, the lattice-distortion induced superconductivity in DSMs of Cd_3As_2[27–29] and Au_2Pb[30–34] is reported. For Cd_3As_2, it does not show any superconductivity at the ambient pressure until 1.8 K[27–29]. The structural phase transition occurs near 2.6 GPa from a tetragonal lattice with D_{4h} point group symmetry ($I4_1/acd$) to a monoclinic lattice with C_{2h} point group symmetry ($P2_1/c$). Then, superconductivity emerges at $T_c \approx 1.8$ K under pressure higher than 8.5 GPa. When the pressure increases further, T_c keeps increasing from 1.8 K to 4.0 K in the hydrostatic pressure experiment[28]. Similarly, Au_2Pb shows superconductivity at $T_c \approx 1.2$ K after a structural phase transition from the cubic with O_h symmetry ($Fd3m$) to the orthorhombic lattice with D_{2h} symmetry ($Pbnc$)[30,32,34]. T_c increases up to 4 K at 5 GPa, then decreases with further compression[34]. For both materials, the point-contact

[1]Center for Correlated Electron Systems, Institute for Basic Science (IBS), Seoul 08826, Korea. [2]Department of Physics and Astronomy, Seoul National University, Seoul 08826, Korea. [3]Department of Physics and Research Institute for Natural Science, Hanyang University, Seoul 04763, Korea. [4]Institute for High Pressure, Hanyang University, Seoul 04763, Korea. [5]Department of Physics, Incheon National University, Incheon 22012, Korea. [6]Department of Physics, University of Seoul, Seoul 02504, Korea. [7]Natural Science Research Institute, University of Seoul, Seoul 02504, Korea. [8]Center for Theoretical Physics (CTP), Seoul National University, Seoul 08826, Korea. [9]These authors contributed equally: Sangmo Cheon and Ki Hoon Lee. ✉email: sbchung0@uos.ac.kr; bjyang@snu.ac.kr

measurements reported that measured T_c using a hard contact tip is much higher than the measured T_c using a soft tip[27,29,32]. The point-contact measurements for Cd_3As_2 showed the zero-bias conductance peak (ZBCP) and double conductance peaks symmetric around zero bias, which was interpreted as a signal of a topological Majorana surface state[27,29]. Moreover, the transport data under magnetic fields reported anomalous behaviors that the conventional BCS theory cannot explain[27,29,32]. At ambient pressure, the proximity-induced superconductivity in Cd_3As_2 is also reported[35].

In parallel to the experimental exploration of the superconductivity in doped DSM, several theoretical studies were conducted[36,37]. In the absence of lattice distortion, the possible superconducting states in doped DSM are suggested as either fully-gapped superconductor (FGSC) or topological nodal superconductor (TNSC) hosting a flat surface Andreev bound state (SABS) on the boundary[37]. In experiments, however, superconductivity was observed only in the presence of lattice distortion. Considering a lattice distortion (in our work, n_1 type lattice distortion), the topological crystalline superconductor (TCSC) hosting surface Majorana states was proposed[36]. However, because such lattice distortion results in the orthorhombic lattice, it cannot be applied to the observed superconductivity in the monoclinic crystal structure of Cd_3As_2[28]. It is, therefore, necessary to study the effect of symmetry-lowering lattice distortions on the emergence of unconventional superconductivity in doped DSM.

In this work, we systematically study possible symmetry-lowering lattice distortions and their effects on the emergence of unconventional superconductivity in doped topological DSM. As a representative model, we consider a topological DSM described by the four-band Hamiltonian having D_{4h} point group symmetry in the absence of lattice distortions. While keeping time-reversal symmetry (TRS) and inversion symmetry (IS), we find four types of symmetry-lowering lattice distortions from the group-theoretical analysis, which are denoted as n_i type lattice distortions ($i = 1, \ldots, 4$). Two of them (n_1 and n_2 type) reduce D_{4h} of the tetragonal lattice to D_{2h} orthorhombic lattice, while the others (n_3 and n_4 type) transform the tetragonal lattice to C_{2h} of the monoclinic lattice. They explain the structural phase transition in Cd_3As_2 and Au_2Pb under pressure. The symmetry-lowering lattice distortions are summarized in Table 3.

To understand the emergence of superconductivity under lattice distortions, we adopt the Bogoliubov-de Gennes (BdG) formalism and linearized gap equation, and we assume intra-orbital (U) and inter-orbital (V) electron density-density interactions which induce superconducting instabilities. From the Fermi-Dirac statistics, six possible momentum-independent superconducting pairing potentials are found[37]. Under lattice distortions, six pairings potentials are classified according to the irreducible representation of the remaining point symmetry group. Using these pairing potentials, possible superconducting gap structures and superconducting critical temperatures (T_c) are calculated. By comparing critical temperatures, we obtain the superconducting phase diagram, and the dominant superconducting phases are discovered, such as fully-gapped superconductor (FGSC), topological nodal superconductor (TNSC), and topological crystalline superconductor (TCSC) depending on the lattice distortions and the ratio of U/V. Among them, FGSC is conventional superconductor, while TNSC and TCSC are unconventional.

Interestingly, the unconventional superconductors of TNSC and TCSC emerge when inter-orbital interaction V and the strength of lattice distortion are large enough while FGSC emerges in the opposite limit. Therefore, the lattice distortion and inter-orbital interaction act as physical parameters that control the phase transition between conventional and unconventional superconductivity of a topological DSM. We find that both V and lattice distortions enhance the unconventional superconducting pairings via a unique spin-orbit locking. Moreover, T_c increases under the lattice distortions due to the enhancement of DOS at the Fermi surface, which is consistent with the experimentally measured T_c enhancement under pressure. The unconventional superconductors host gapless SABS in mirror plane even under the lattice distortions: Under the n_1 or n_2 type lattice distortion, the superconductivity in the orthorhombic lattice with D_{2h} point group symmetry hosts a gapless SABS protected by the mirror Chern number. Under the n_3 or n_4 type lattice distortion, the superconductivity in the monoclinic lattice with C_{2h} point group symmetry hosts a gapless SABS protected by the unbroken mirror symmetry and a flat SABS protected by the mirror chiral winding number in specific conditions. Because there exist gapless Majorana surface states under the lattice distortions, we suggest that these states can be observed in scanning tunneling microscope (STM) or point contact Andreev reflection spectroscopy experiments.

Consequently, our theoretical work is consistent with the discovered structural phase transition and the enhancement of superconductivity in Cd_3As_2 and Au_2Pb under lattice distortions. Moreover, we suggest that the emergence of conventional and unconventional superconductivity in doped topological DSM can be controlled by the pressure and strength of the superconducting pairing interaction. Therefore, our woks opens a pathway to explore and control the topological superconductors in doped topological semimetals, which may have future applications in dissipationless and quantum information devices.

Results

Undistorted Dirac semimetal. Dirac semimetal (DSM) has the low energy excitations near the Fermi-level described by a massless Dirac equation. Because all bands are doubly degenerate due to the TRS and IS, a DSM is minimally described by a four-band Hamiltonian[6,10,38–40]. However, TRS and IS are not enough to protect a fourfold degeneracy, so the symmetry-protected DSM is suggested, where the Dirac points are protected by TRS, IS and crystalline symmetries[6,10,38–40]. DSMs are reported in many materials such as β-cristobalite BiO_2 [10], distorted spinels[41], Na_3Bi[42,43], Cd_3As_2[42,44–49], Au_2Pb[30,50], and $ZrTe_5$[51,52]. Among them, superconductivity is reported in Cd_3As_2[27–29] and Au_2Pb[30–34]. Both materials have Dirac points protected by TRS, IS, and C_4 rotational symmetry and share the tetragonal crystal system with D_{4h} point group symmetry. For this reason, we consider the undistorted topological DSM having a D_{4h} point group symmetry as a representative model system.

Model and symmetry. The general 4×4 Hamiltonian representation is

	IR	T	P	C_{4z}	M_{xy}	M_{yz}	M_{xz}	$M_{(110)}$	$M_{(1\bar{1}0)}$
Γ_0, Γ_5	A_{1g}	+	+	+	+	+	+	+	+
Γ_4	B_{1u}	−	−	−	−	−	−	+	+
Γ_3	B_{2u}	−	−	−	−	+	+	−	−
(Γ_1, Γ_2)	E_u	$(-,-)$	$(-,-)$	$(\Gamma_2, -\Gamma_1)$	$(+,+)$	$(-,+)$	$(+,-)$	$(-\Gamma_2, -\Gamma_1)$	(Γ_2, Γ_1)

Table 1. Transformation properties of gamma matrices under symmetry operations. Under an operation O, each gamma matrices satisfies the relation of $O\Gamma_i O^{-1} = \pm\Gamma_j$. In each entry, if $i = j$, the overall sign is written, otherwise the explicit form is given. The gamma matrices are classified according to the irreducible representation (IR) of D_{4h} point group. Γ_0, Γ_5, Γ_4, and Γ_3 belong to the A_{1g}, A_{1g}, B_{1u}, and B_{2u} irreducible representations, respectively. Γ_1 and Γ_2 belong to the two-dimensional E_u irreducible representation.

	T	P	C_{4z}	M_{xy}	M_{yz}	M_{xz}	$M_{(110)}$	$M_{(1\bar{1}0)}$
$a_0(S\mathbf{k}), a_5(S\mathbf{k})$	+	+	+	+	+	+	+	+
$(a_1(S\mathbf{k}), a_2(S\mathbf{k}))$	$(-,-)$	$(-,-)$	$(-a_2(\mathbf{k}), a_1(\mathbf{k}))$	$(+,+)$	$(-,+)$	$(+,-)$	$(-a_2(\mathbf{k}), -a_1(\mathbf{k}))$	$(a_2(\mathbf{k}), a_1(\mathbf{k}))$
$a_3(S\mathbf{k})$	−	−	−	−	+	+	−	−
$a_4(S\mathbf{k})$	−	−	−	−	−	−	+	+

Table 2. Symmetry constraints on $a_i(\mathbf{k})$. They are determined by Eq. (5). If the coefficient function is proportional to itself, $a_i(S\mathbf{k}) = \pm a_i(\mathbf{k})$, the overall sign is denoted. If not, the explicit form is denoted.

$$H(\mathbf{k}) = \sum_{i=1}^{16} a_i(\mathbf{k})\Gamma_i. \tag{1}$$

The coefficient function $a_i(\mathbf{k})$ are real functions and $\Gamma_i = s_j\sigma_k$ are 4×4 gamma matrices where s_j and σ_k are Pauli matrices for spin and orbital degrees of freedom in the spin $(\uparrow, \downarrow)$ and the orbital $(1, 2)$ spaces, respectively.

The symmetry constraints can simplify the Hamiltonian's form in Eq. (1). Due to TRS and IS, the Hamiltonian satisfies the following equations:

$$TH(\mathbf{k})T^{-1} = H(-\mathbf{k}), \quad PH(\mathbf{k})P^{-1} = H(-\mathbf{k}), \tag{2}$$

where $T = is_y\hat{K}$ is the time-reversal operator ($\hat{K}$ is the complex conjugation operator) and P is the inversion operator. Because the inversion does not flip the spin, the inversion operator has orbital dependency only, and it can be chosen as $P = -\sigma_z$ for topological DSM without loss of generality[39,45]. Then, due to TRS and IS, among sixteen Γ_i matrices, only six Γ_i matrices are allowed. They are $\Gamma_0 = \mathbf{1}_{4\times4}$, $\Gamma_1 = \sigma_x s_z$, $\Gamma_2 = \sigma_y s_0$, $\Gamma_3 = \sigma_x s_x$, $\Gamma_4 = \sigma_x s_y$, and $\Gamma_5 = \sigma_z s_0$. We set $a_0(\mathbf{k}) = 0$ since it does not contribute to the formation of Dirac points[39,45].

The D_{4h} point group symmetry imposes more constraints on the Hamiltonian's form in Eq. (1). The generators of D_{4h} point group can be chosen as inversion P, fourfold rotation about the z axis C_{4z}, and twofold rotation about the x axis C_{2x}. Their matrix representations are chosen as

$$P = -\sigma_z, \quad C_{4z} = \exp(-i\frac{\pi}{2}s_z - i\frac{\pi}{4}\sigma_z s_z), \quad C_{2x} = i\sigma_z s_x, \tag{3}$$

where we adopt the following basis set known to describe the low-energy effective Hamiltonian of Cd_2As_3[45].

$$|1,\uparrow\rangle = \left|P_{J=\frac{3}{2}}, 3/2\right\rangle, \quad |1,\downarrow\rangle = \left|P_{J=\frac{3}{2}}, -3/2\right\rangle, \quad |2,\uparrow\rangle = \left|S_{J=\frac{1}{2}}, 1/2\right\rangle, \quad |2,\downarrow\rangle = \left|S_{J=\frac{1}{2}}, -1/2\right\rangle, \tag{4}$$

where J is the total angular momentum. Other rotation and mirror symmetries are given by $C_{2z} = i\sigma_z s_z$, $M_{xy} = -is_z$, $M_{yz} = -is_x$, $M_{zx} = -i\sigma_z s_y$, $M_{(110)} = i(\sigma_z s_x - s_y)/\sqrt{2}$, and $M_{(1\bar{1}0)} = i(\sigma_z s_x + s_y)/\sqrt{2}$. The subscript in each mirror operator represents the corresponding mirror plane by using either Cartesian coordinates or Miller indices. The group elements are derived in Sec. S1 in Supplementary Information. Due to this D_{4h} symmetry, the Hamiltonian in Eq. (1) satisfy

$$UH(\mathbf{k})U^{-1} = H(S\mathbf{k}), \tag{5}$$

where U and S are transformation matrices for an element of D_{4h} group in the spin-orbital and momentum spaces, respectively. For the group generators, the Hamiltonian in Eq. (1) satisfies

$$PH(\mathbf{k})P^{-1} = H(-\mathbf{k}), \quad C_{4z}H(\mathbf{k})C_{4z}^{-1} = H(\mathscr{R}_{4z}\mathbf{k}), \quad C_{2x}H(\mathbf{k})C_{2x}^{-1} = H(\mathscr{R}_{2x}\mathbf{k}), \tag{6}$$

where $\mathscr{R}_{4z}\mathbf{k} = (-k_y, k_x, k_z)$ and $\mathscr{R}_{2x}\mathbf{k} = (k_x, -k_y, -k_z)$. Because the transformation properties of gamma matrices are given by Table 1, Eq. (5) imposes constraints to each coefficient functions $a_i(\mathbf{k})$, which is summarized in Table 2. Therefore, the general form of the Hamiltonian of DSM having D_{4h} point group symmetry is obtained.

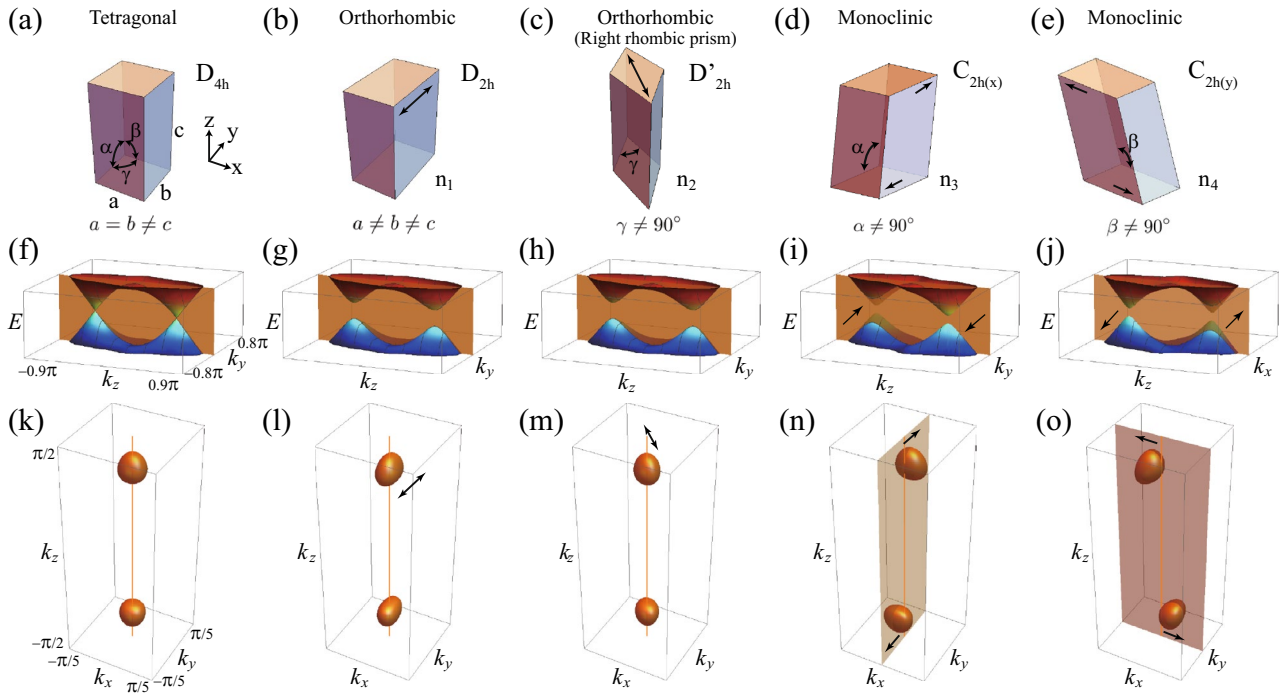

Figure 1. Crystal systems, band structures, and Fermi surfaces of Dirac semimetal (DSM) under various lattice distortions. (**a**) Undistorted DSM for comparison. It has a tetragonal lattice. (**b**–**e**) Distorted crystal systems under (**b**) n_1, (**c**) n_2, (**d**) n_3, and (**e**) n_4 type lattice distortions. In (**b**) and (**c**), n_1 and n_2 type lattice distortions changes inplane lattice constants, which results in orthorhombic lattices. In (**d**) and (**e**), n_3 and n_4 type lattice distortions change the α and β angles, which results in monoclinic lattices. (**f**–**j**) The corresponding 3D band structures. In (**f**–**i**) [(**j**)], the band structures are plotted for the k_y-k_z (k_x-k_z) plane and the orange planes are $k_y = 0$ ($k_x = 0$) plane. (**k**–**o**) The corresponding Fermi surfaces. In (**l**–**o**), all Fermi surfaces are distorted according to types of lattice distortions. In (**n**) and (**o**), the Fermi surfaces are shifted as indicated by the black arrows. Each vertical orange line indicates the k_z axis.

Lattice model. For concreteness, we construct an explicit lattice model that describes a class of Dirac semimetals such as Cd_3As_2 and Au_2Pb. The coefficient functions of Hamiltonian in Eq. (1) are given by[39,45]

$$a_1(\mathbf{k}) = v \sin k_x, \tag{7}$$

$$a_2(\mathbf{k}) = v \sin k_y, \tag{8}$$

$$a_3(\mathbf{k}) = (\beta + \gamma) \sin k_z (\cos k_y - \cos k_x), \tag{9}$$

$$a_4(\mathbf{k}) = -(\beta - \gamma)(\sin k_z \sin k_x \sin k_y), \tag{10}$$

$$a_5(\mathbf{k}) = M' - t_{xy}(\cos k_x + \cos k_y) - t_z \cos k_z, \tag{11}$$

where M', t_{xy}, t_z, v, β, and γ are material-dependent parameters. The energy eigenvalues are given by

$$E = \pm|a(\mathbf{k})| = \pm\left(\sum_{i=1}^{5} a_i^2(\mathbf{k})\right)^{1/2}. \tag{12}$$

If $t_z > (M' - 2t_{xy}) > 0$, the Hamiltonian hosts a pair of Dirac points at $(0, 0, \pm k_0)$ as shown in Fig. 1a. Here, k_0 is determined by $M' - 2t_{xy} - t_z \cos k_0 = 0$. These Dirac points are protected by the C_{4z} symmetry[39]. Due to the C_{4z}, the four bands on the k_z axis can have different C_{4z} eigenvalues, which lead to fourfold degenerate Dirac points.

Low-energy effective Hamiltonian. Near the Dirac points $(0, 0, \pm k_0)$, the low-energy effective Hamiltonian takes the form of Dirac Hamiltonian, which is given by

$$H_{\text{Dirac}}^{(\pm)} = vk_x\Gamma_1 + vk_y\Gamma_2 \pm v_z(k_z \mp k_0)\Gamma_5. \tag{13}$$

where $v_z = t_z k_0$. The energy spectrum shows anisotropic energy-momentum dispersion, which is given by

Type	Form	Remaining subgroup	Essential elements	Material
n_1	$\sin k_z \Gamma_3$	D_{2h}	$C_{2z}, M_{xy}, M_{xz}, M_{yz}$	Au_2Pb
n_2	$\sin k_z \Gamma_4$	D'_{2h}	$C_{2z}, M_{xy}, M_{(110)}, M_{(1\bar{1}0)}$	Au_2Pb
n_3	$\sin k_z \Gamma_2$	$C_{2h(x)}$	C_{2x}, M_{yz}	Cd_3As_2
n_4	$\sin k_z \Gamma_1$	$C_{2h(y)}$	C_{2y}, M_{xz}	Cd_3As_2

Table 3. Four types of symmetry-lowering lattice distortions are classified according to the irreducible representation of D_{4h} point group. n_1 and n_2 belong to the B_{1g} and B_{2g} irreducible representations of D_{4h}, respectively, while n_3 and n_4 belong to the two-dimensional E_g irreducible representation. For each lattice distortion, the matrix form, remaining essential group elements, and related material are listed.

$$E = \pm\sqrt{v^2(k_x^2 + k_y)^2 + v_z^2(k_z \mp k_0)^2}. \tag{14}$$

Distorted Dirac semimetal. *Symmetry-lowering distortions.* In the absence of lattice distortions, Cd_3As_2[27–29] and Au_2Pb[32–34] share the same D_{4h} point group symmetry and show no superconductivity. However, both materials showed superconductivity after the structural phase transition under pressure or cooling, and the superconducting critical temperature increases with the pressure[28,34]. At the high pressure, Cd_3As_2 becomes a monoclinic lattice having C_{2h} point group symmetry[28] and Au_2Pb becomes an orthorhombic lattice having D_{2h} point group symmetry[32]. Thus, IS is preserved even under lattice distortions. In addition, the superconductivity appears under the small lattice distortions in the hydrostatic experiments[28,34]. Therefore, we assume that both TRS and IS are preserved under lattice distortions and the effect of the lattice distortion can be implemented as a perturbation[53].

We now classify the possible symmetry-lowering lattice distortions. The form of the perturbation Hamiltonian for the lattice distortions is given by

$$H_{\text{pert}} = \sum_{i=0}^{5} d_i(\mathbf{k})\Gamma_i, \tag{15}$$

where $d_i(\mathbf{k})$ is a real-valued function of momentum and Γ_i is the gamma matrix. Because Γ_1, Γ_2, Γ_3, and Γ_4 are odd under T and P, the coefficient functions $d_1(\mathbf{k})$, $d_2(\mathbf{k})$, $d_3(\mathbf{k})$, and $d_4(\mathbf{k})$ are odd functions with respect to $\mathbf{k}$. Similarly, the coefficient functions $d_0(\mathbf{k})$ and $d_5(\mathbf{k})$ are even functions with respect to $\mathbf{k}$. Thus, the allowed lattice distortion terms can be either $k^{\text{odd}}\ \Gamma_{1,2,3,4}$ or $k^{\text{even}}\ \Gamma_{0,5}$ types.

Because we assume TRS and IS to remain under lattice distortions, the Hamiltonians for distorted and undistorted DSM have the same form of $H = \sum_i a_i(\mathbf{k})\Gamma_i$. The only difference between the two Hamiltonians is the transformation properties of the coefficient function $a_i(\mathbf{k})$. In the absence of lattice distortions, $a_i(\mathbf{k})$ needs to satisfy all transformation properties under all symmetry operations of D_{4h} point group in Table 2. However, in the presence of lattice distortion, $a_i(\mathbf{k})$ only needs to satisfy the transformation properties under the remaining symmetry operations, so $a_i(\mathbf{k})$ is less constrained.

Lattice Hamiltonian with lattice distortions. To discuss the effect of lattice distortions explicitly, we introduce the possible symmetry-lowering lattice distortions in the lattice model in Eqs. (7-11). For weak lattice distortions, the lattice distortions are approximately proportional to $\sin k_i$ and $\cos k_i$ as only nearest neighbor hoppings are relevant. Because we are interested in the Dirac physics near the Dirac points $(0, 0, \pm k_0)$, we assume that $k_x/k_z \ll 0$ and $k_y/k_z \ll 0$, which implies that $\sin k_x$ and $\sin k_y$ are smaller than $\sin k_z$ and $\cos k_i$. Hence, $\sin k_z$ and $\cos k_i$ are dominant momentum dependent terms in the leading order, and the allowed lattice distortions are either $\sin k_z\ \Gamma_{1,2,3,4}$ or $\cos k_i\ \Gamma_{0,5}$ types. Because $\cos k_i\ \Gamma_{0,5}$ types are included in the trivial A_{1g} class of D_{4h} point group, they do no break any symmetry. On the other hand, $\sin k_z\ \Gamma_{1,2,3,4}$ types are included in B_{1g}, B_{2g}, and E_g, and they break the crystal symmetry properly, which are summarized in Table 3. Therefore, in the leading order, there are four types of symmetry-lowering lattice distortion, which are given by

$$H_{\text{pert}} = \sin k_z(n_1\Gamma_3 + n_2\Gamma_4 + n_3\Gamma_2 + n_4\Gamma_1), \tag{16}$$

where n_i is the strength of each lattice distortion. For convenience, each lattice distortion is denoted as n_i type lattice distortions in this work. From now on, we will consider these four types of symmetry-lowering lattice distortions, and the possible higher-order terms are discussed in Sec. S2 in Supplementary Information.

Therefore, the coefficient functions in Eq. (1) are given by

$$
\begin{aligned}
a_1(\mathbf{k}) &= v \sin k_x + n_4 \sin k_z, \\
a_2(\mathbf{k}) &= v \sin k_y + n_3 \sin k_z, \\
a_3(\mathbf{k}) &= (\beta + \gamma)(\cos k_y - \cos k_x) \sin k_z + n_1 \sin k_z, \\
a_4(\mathbf{k}) &= -(\beta - \gamma)(\sin k_x \sin k_y \sin k_z) + n_2 \sin k_z, \\
a_5(\mathbf{k}) &= M' - t_{xy}(\cos k_x + \cos k_y) - t_z \cos k_z.
\end{aligned} \tag{17}
$$

Under lattice distortion, the fourfold rotation symmetry is broken. Thus, the Dirac point is gapped, which can be seen from the energy eigenvalues on the k_z axis, $E = \pm\sqrt{(n_1^2 + n_2^2 + n_3^2 + n_4^2)\sin^2 k_z + a_5(0,0,k_z)^2}$. Thus, the Dirac point is gapped unless $n_1^2 + n_2^2 + n_3^2 + n_4^2 = 0$. As a result of the gap-opening, the DSM becomes a 3D topological insulator because of the band inversion at the Γ point[36,39]. Counting all the parity eigenvalues for the time-reversal-invariant momenta (TRIM) points of the bulk Brillouin zone (BZ)[1,54] gives a nontrivial $\mathbb{Z}_2$ invariant.

The effect of lattice distortions. The four types of symmetry-lowering lattice distortions in Eq. (16) are classified according to the irreducible representation of D_{4h} group. The symmetry-lowering lattice distortions break D_{4h} point group symmetry into its subgroup symmetry, which is summarized in Table 3. The n_1 and n_2 type lattice distortions are included in the one-dimensional class B_{1g} and B_{2g}, and break D_{4h} point group symmetry into D_{2h} and D'_{2h}, respectively. The n_3 and n_4 type lattice distortions are included in the two-dimensional class E_u and break D_{4h} point group symmetry into C_{2h}. Note that n_2 type lattice distortion is related to the n_1 type lattice distortion via $\pi/4$ rotation, while n_4 type lattice distortion is related to the n_3 type lattice distortion via $\pi/2$ rotation.

We investigate the explicit effects of the lattice distortions on the crystal systems and the Fermi surfaces using the lattice model in Eq. (17). Figure 1 shows the crystal structures, the 3D band structures, and Fermi surfaces under various lattice distortions. Under n_1 type lattice distortion, the crystal system and Fermi surface are elongated along x or y direction, C_{4z} symmetry is broken, the Dirac point is gapped, and the crystal system becomes orthorhombic (Fig. 1b, g). Similarly, under the n_2 type lattice distortion, the crystal system and Fermi surface are elongated along diagonal lines either $x = y$ or $x = -y$, C_{4z} symmetry is broken, the Dirac point is gapped, and the crystal system becomes orthorhombic (Fig. 1c, h). We denote the symmetry point group of this right rhombic prism as D'_{2h}. Under n_3 type lattice distortion, the crystal structure undergoes structural phase transition from tetragonal to monoclinic (Fig. 1d). Two Dirac points in the band structure are shifted oppositely along k_y direction and the centers of each Fermi surfaces are also oppositely shifted along the same k_y direction (Fig. 1h). Similar effects occur under n_4 type lattice distortion (Fig. 1e, j) because n_4 type lattice distortion are related with the n_3 type lattice distortion via $\pi/2$ rotation. The point groups of these distorted systems under n_3 and n_4 type lattice distortions are denoted as $C_{2h(x)}$ and $C_{2h(y)}$, respectively. Therefore, the four types of symmetry-lowering lattice distortions explain the lattice distortions of Cd_3As_2 and Au_2Pb under pressure.

Low-energy effective Dirac Hamiltonian under lattice distortions. Near the Dirac points $(0, 0, \pm k_0)$, the coefficient functions of the low-energy effective Hamiltonian can be approximated as

$$
\begin{aligned}
a_1(\mathbf{k}) &= vk_x + n_4 \sin k_0, \\
a_2(\mathbf{k}) &= vk_y + n_3 \sin k_0, \\
a_3(\mathbf{k}) &= (\beta + \gamma)\left(\frac{k_x^2 - k_y^2}{2}\right) \sin k_0 + n_1 \sin k_0, \\
a_4(\mathbf{k}) &= -(\beta - \gamma)k_x k_y \sin k_0 + n_2 \sin k_0, \\
a_5(\mathbf{k}) &= \pm v_z(k_z \mp k_0)\sigma_z.
\end{aligned}
$$

With this low-energy effective Hamiltonian, we show that the lattice distortion acts as a Dirac mass term and increases DOS at Fermi surface. We assume that the Fermi level is slightly above the Dirac points in undistorted lattice, or near the bottom of the conduction band minima after gap-opening at the Dirac points.

For n_1 and n_2 type lattice distortions, the low-energy effective Hamiltonian is given by

$$
H_{\text{Dirac}}^{(\pm)} = vk_x\Gamma_1 + vk_y\Gamma_2 \pm v_z(k_z \mp k_0)\Gamma_5 \pm n_1 \sin k_0\Gamma_3 \pm n_2 \sin k_0\Gamma_4. \tag{18}
$$

So, n_1 and n_2 type lattice distortion terms act as Dirac mass terms. The energy eigenvalue is given by

$$
E = \pm\sqrt{v^2(k_x^2 + k_y^2) + v_z^2(k_z \mp k_0)^2 + |n|^2 \sin^2 k_0}, \tag{19}
$$

where $|n| = \sqrt{n_1^2 + n_2^2}$. By the assumption of the total electron number conservation under a weak lattice distortion, the lattice distortion dependent DOS at the Fermi surface is given by

$$
\text{DOS}(|n|) = \frac{1}{\pi v^2 v_z}\mu_0\sqrt{\mu_0^2 + |n|^2 \sin^2 k_0}, \tag{20}
$$

which indicates that DOS at the Fermi level is enhanced under the lattice distortion. Here, μ_0 indicates the chemical potential of the undistorted lattice. See the detailed derivations in Sec. S2.4 in Supplementary Information.

Next, we consider the n_3 type lattice distortion. The n_3 type lattice distortion shifts the gap minima along the k_y direction from $(0,0,\pm k_0)$ to $(0,\pm k_y^{(0)},\pm k_0)$ with $k_y^{(0)} = -n_3 \sin k_0/v$. Then, the low-energy effective Hamiltonian near the gap minima points $(0,\pm k_y^{(0)},\pm k_0)$ is given by

$$H_{\text{Dirac}}^{(\pm)} = vk_x\Gamma_1 + v(k_y \mp k_y^{(0)})\Gamma_2 \pm v_z(k_z \mp k_0)\Gamma_5 \pm m\Gamma_3,$$

where $m = -(\beta+\gamma)\frac{n_3^2 \sin^3 k_0}{2v^2}$ is the Dirac mass term. The energy eigenvalue is given by

$$E = \pm\sqrt{v^2k_x^2 + v^2(k_y \mp k_y^{(0)})^2 + v_z^2(k_z \mp k_0)^2 + m^2}. \tag{21}$$

Similar to n_1 and n_2 type lattice distortions, DOS at the Fermi surface are given by

$$\text{DOS}(n_3) = \frac{1}{\pi v^2 v_z}\mu_0\sqrt{\mu_0^2 + m^2}, \tag{22}$$

which means that the DOS at the Fermi level is enhanced under n_3 type lattice distortion. Similarly, for n_4 type lattice distortion, the low-energy effective Hamiltonian and DOS are easily calculated because n_3 and n_4 type lattice distortions are related via $\pi/2$ rotation.

Multiple symmetry-lowering lattice distortions. So far, we have considered only one type of lattice distortions. However, more than two types of lattice distortions can be turned on simultaneously. In this case, the final subgroup symmetry determines the crystal system and its physical properties. When both n_1 and n_3 types lattice distortions are turned on, the remaining subgroup has P, C_{2x}, M_{yz} symmetries. This subgroup is the same point group of the distorted Dirac semimetal under single n_3 type lattice distortion. In other words, under n_3 type lattice distortion, the addition of n_1 type lattice distortion is also allowed. A similar argument can be applied to n_2 and n_4 types lattice distortions. When both n_1 and n_2 type lattice distortions are turned on, the remaining symmetries are P, C_{2z}, M_{xy} symmetries. We denote this point subgroup as $C_{2h(z)}$, and we will not consider this case seriously because there is no real material that corresponds to this case. Similarly, the other combinations such as $(n_2,n_3), (n_1,n_4), (n_3,n_4), (n_1,n_2,n_3), (n_1,n_2,n_4)$ break all crystal symmetries except the inversion, and hence these cases are not interested in this work.

Superconductivity. *BdG Hamiltonian.* To discuss the effects of lattice distortions on the superconductivity in doped DSM, we construct the Bogoliubov-de Gennes (BdG) Hamiltonian within mean-field approximation while keeping TRS and the crystal symmetry[55,56]. The BdG Hamiltonian is given by

$$H_{\text{BdG}} = \int d\mathbf{k}\,\Psi_{\mathbf{k}}^\dagger \mathscr{H}(\mathbf{k})\Psi_{\mathbf{k}}, \tag{23}$$

$$\mathscr{H}(\mathbf{k}) = [H(\mathbf{k}) - \mu]\tau_z + \Delta(\mathbf{k})\tau_x, \tag{24}$$

where τ_i is the Pauli matrices in the Nambu space. $\Delta(\mathbf{k})$ and μ are a pairing potential and a chemical potential, respectively. $H(\mathbf{k})$ is the normal state Hamiltonian in Eq. (1). The basis is taken as

$$\Psi_{\mathbf{k}}^\dagger = (c_{1\mathbf{k}\uparrow}^\dagger, c_{2\mathbf{k}\uparrow}^\dagger, c_{1\mathbf{k}\downarrow}^\dagger, c_{2\mathbf{k}\downarrow}^\dagger, c_{1-\mathbf{k}\downarrow}, c_{2-\mathbf{k}\downarrow}, -c_{1-\mathbf{k}\uparrow}, -c_{2-\mathbf{k}\uparrow}). \tag{25}$$

While the pairing mechanism of doped DSM is not known yet, we assume the following onsite density-density interaction as a superconducting pairing interaction[36,37,57,58]:

$$H_{\text{int}}(x) = -U[n_1^1(x) + n_2^2(x)] - 2Vn_1(x)n_2(x), \tag{26}$$

where $n_i(x)$ is the electron density operators for ith orbital ($i = 1, 2$). U and V are intra-orbital and inter-orbital interaction strengths, respectively, and we assume that at least one of them is attractive and responsible for superconductivity. Because the pairing interaction depends on the orbital and is local in $\mathbf{x}$, the mean-field pairing potential is orbital dependent but momentum independent: $\Delta(\mathbf{k}) = \Delta$.

Symmetry of BdG Hamiltonian. The BdG Hamiltonian in Eq. (23) has time-reversal symmetry T, particle-hole symmetry C, and chiral symmetry Γ:

$$T\mathscr{H}(\mathbf{k})T^{-1} = \mathscr{H}(-\mathbf{k}), \tag{27}$$

$$C\mathscr{H}(\mathbf{k})C^{-1} = -\mathscr{H}(-\mathbf{k}), \tag{28}$$

$$\Gamma\mathscr{H}(\mathbf{k})\Gamma^{-1} = \mathscr{H}(\mathbf{k}), \tag{29}$$

where $T = is_y\sigma_0\tau_0\hat{K}$ and $C = is_y\sigma_0\tau_y\hat{K}$ are time-reversal and particle-hole symmetry operators, respectively, and $\Gamma = TC = s_0\sigma_0\tau_y$ is the chiral operator. $\hat{K}$ is the complex conjugation operator. Therefore, the BdG Hamiltonian belongs to in DIII class according to the classification table of topological insulator and superconductor[59].

If the pairing potential satisfies $P\Delta(\mathbf{k})P^{-1} = \eta_P\Delta(-\mathbf{k})$, the BdG Hamiltonian has the inversion symmetry:

Pairing	D_{4h}	E	P	C_{4z}	C_{2x}	M_{xy}	M_{yz}	M_{zx}	M_{110}	$M_{1\bar{1}0}$	Fermion bilinear	Matrix form
Δ_1	A_{1g}	1	1	1	1	1	1	1	1	1	$c^\dagger_{1\uparrow}c^\dagger_{1\downarrow}+c^\dagger_{2\uparrow}c^\dagger_{2\downarrow}+h.c.$	$\hat{I}$
Δ_1'	A_{1g}	1	1	1	1	1	1	1	1	1	$c^\dagger_{1\uparrow}c^\dagger_{1\downarrow}-c^\dagger_{2\uparrow}c^\dagger_{2\downarrow}+h.c.$	σ_z
Δ_2	B_{1u}	1	−1	−1	1	−1	−1	−1	1	1	$c^\dagger_{1\uparrow}c^\dagger_{2\uparrow}+c^\dagger_{1\downarrow}c^\dagger_{2\downarrow}+h.c.$	$\sigma_y s_y$
Δ_3	B_{2u}	1	−1	−1	−1	−1	1	1	−1	−1	$i(c^\dagger_{1\uparrow}c^\dagger_{2\uparrow}-c^\dagger_{1\downarrow}c^\dagger_{2\downarrow})+h.c.$	$\sigma_y s_x$
Δ_{41}	E_u	1	−1	Δ_{42}	−1	1	1	−1	Δ_{42}	-Δ_{42}	$c^\dagger_{1\uparrow}c^\dagger_{2\downarrow}-c^\dagger_{1\downarrow}c^\dagger_{2\uparrow}+h.c.$	σ_x
Δ_{42}	E_u	1	−1	-Δ_{41}	1	1	−1	1	Δ_{41}	-Δ_{41}	$i(c^\dagger_{1\uparrow}c^\dagger_{2\downarrow}+c^\dagger_{1\downarrow}c^\dagger_{2\uparrow})+h.c.$	$\sigma_y s_z$

Table 4. The pairing potentials are classified according to the irreducible representation of D_{4h} point group. Δ_1, Δ_1', Γ_2, and Γ_3 belong to the A_{1g}, A_{1g}, B_{1u}, and B_{2u} irreducible representations, respectively. Δ_{41} and Γ_{42} belong to the two-dimensional E_u irreducible representation. The transformation properties of the pairing potentials are represented by +1 and −1 for even and odd parities. For two-dimensional representation E_u, the explicit forms are listed.

$$\tilde{P}\mathscr{H}(\mathbf{k})\tilde{P}^{-1}=\mathscr{H}(-\mathbf{k}),\quad \text{with}\ \ \tilde{P}=\text{diag}(P,\eta_P P), \tag{30}$$

where P and $\tilde{P}$ are the inversion operators for the DSM and BdG Hamiltonians, respectively, and η_P is the inversion parity. If $\eta_P=1$ ($\eta_P=-1$), the superconducting phase is an inversion-even-parity (inversion-odd-parity) superconductor. For a single-orbital superconductor, $\tilde{P}$ is the identity operator, and an inversion-odd-parity (inversion-even-parity) pairing is equivalent to the spin-triplet (spin-singlet) pairing. However, because of the spin-orbit coupling and multi-orbital band structure, the pairings are more complex in our case.

From now on, we consider momentum independent pairing potentials, $\Delta(\mathbf{k})=\Delta$, because we assume onsite pairing interaction as discussed in Eq. (26). In the absence of lattice distortions, the BdG Hamiltonian has D_{4h} point group symmetry[37]. If a pairing potential satisfies the transformation property of $U\Delta s_y U^T s_y=\eta_U\Delta$ under a symmetry operation of D_{4h} point symmetry group, the BdG Hamiltonian satisfies the corresponding symmetry:

$$\tilde{U}\mathscr{H}(\mathbf{k})\tilde{U}^{-1}=\mathscr{H}(S\mathbf{k}), \tag{31}$$

where U is the symmetry operator in spin and orbital spaces, η_U is a phase factor, and $\tilde{U}=\text{diag}(U,\eta_U s_y U^* s_y)$ is the extended symmetry operator in the Nambu space.

For the generators of D_{4h} point group, if the pairing potential satisfies $C_{4z}\Delta s_y C_{4z}^T s_y=\eta_{C_{4z}}\Delta$ with $\eta_{C_{4z}}=e^{i\pi r/2}$ ($r=0,\ldots,3$) and $C_{2x}\Delta s_y C_{2x}^T s_y=\eta_{C_{2x}}\Delta$ with $\eta_{C_{2x}}=\pm1$, then the BdG Hamiltonian satisfies the corresponding rotation symmetry:

$$\tilde{C}_{4z}\mathscr{H}(\mathbf{k})\tilde{C}_{4z}^{-1}=\mathscr{H}(R_{4z}\mathbf{k}), \tag{32}$$

$$\tilde{C}_{2x}\mathscr{H}(\mathbf{k})\tilde{C}_{2x}^{-1}=\mathscr{H}(R_{2x}\mathbf{k}), \tag{33}$$

where the extended symmetry operators are given by $\tilde{C}_{4z}=\text{diag}(C_{4z},\eta_{C_{4z}}s_y C_{4z}^* s_y)$ and $\tilde{C}_{2x}=\text{diag}(C_{2x},\eta_{C_{2x}}s_y C_{2x}^* s_y)$. If the pairing potential satisfies $M\Delta s_y M^T s_y=\eta_M\Delta$ under a mirror operator M, the BdG Hamiltonian satisfies the corresponding mirror symmetry:

$$\tilde{M}\mathscr{H}(\mathbf{k}_\parallel,\mathbf{k}_\perp)\tilde{M}^{-1}=\mathscr{H}(\mathbf{k}_\parallel,-\mathbf{k}_\perp), \tag{34}$$

where $\tilde{M}=\text{diag}\,(M,\eta_M s_y M^* s_y)$ is a mirror operator for BdG Hamiltonian and $\mathbf{k}_\parallel$ ($\mathbf{k}_\perp$) is the momentum vector parallel (perpendicular) to the mirror plane. The η_M is the mirror parity of the pairing potential under the mirror operation M.

In Table 4, the transformation properties of all possible pairing potentials under the rotation and mirror operators are summarized. The details of each pairing potential will be discussed below.

Pairing potentials. We now investigate the possible superconducting pairing potentials in the presence of lattice distortions. Since we are considering multi-orbital superconductivity in the basis of two spins and two orbitals, pairing potentials can be represented as a product of spin Pauli matrices and orbital Pauli matrices, which leads to sixteen matrices. Among them, only six matrices are allowed because of the fermion statistics ($\Delta s_y=s_y\Delta^T$). We denote them as Δ_1, Δ_1', Δ_2, Δ_3, Δ_{41}, and Δ_{42}, whose forms and properties are listed in Table 4. Due to Pauli's exclusion principle, the fermion bilinear form of each pairing potential shows antisymmetric property under the particle exchange. Because the pairing potential is momentum independent, the spatial part is symmetric, while the spin-orbital part is antisymmetric under the particle exchange. Thus, if the spin part is singlet, the orbital part is triplet, and vice versa. Therefore, Δ_1's and Δ_{41} are the spin-singlet orbital-triplet pairings and Δ_2, Δ_3, and Δ_{42} are the spin-triplet orbital-singlet pairings as shown in the bilinear form in Table 4.

Six pairing potentials can be classified according to the irreducible representations of the unbroken point group, and the superconducting critical temperatures for the pairing potentials in the different classes are independent[36,37,56–58]. In the absence of lattice distortions, the pairing potentials are classified according to the

Pairing	D_{4h}	D_{2h}	D'_{2h}	$C_{2h(z)}$	$C_{2h(x)}$	$C_{2h(y)}$
Δ_1	A_{1g}	A_g	A_g	A_g	A_g	A_g
Δ'_1	A_{1g}	A_g	A_g	A_g	A_g	A_g
Δ_2	B_{1u}	A_u	B_{1u}	A_u	A_u	A_u
Δ_3	B_{2u}	B_{1u}	A_u	A_u	B_u	B_u
Δ_{41}	E_u	B_{2u}	$B_{3u} - B_{2u}$	B_u	B_u	A_u
Δ_{42}	E_u	B_{3u}	$B_{3u} + B_{2u}$	B_u	A_u	B_u

Table 5. Pairing potentials classified according to the D_{4h} point group are reclassified according to the irreducible representation of unbroken subgroup under the lattice distortions. For D'_{2h} group, $\Delta_{42} + \Delta_{41}$ and $\Delta_{42} - \Delta_{41}$ pairing potentials belong to in B_{3u} and B_{2u} representations, respectively.

D_{4h} group: Δ_1's, Δ_2, Δ_3 and Δ_4's belong to A_{1g}, B_{1u}, B_{2u} and E_u irreducible representations, respectively, which are summarized in Table 4.

The pairing potential belonging to a specific irreducible representation of the D_{4h} group can be decomposed into a combination of different irreducible representations depending on the symmetry of the distorted lattice. Some pairing potentials in the D_{4h} group's individual representations can be included in the same representation and vice versa. As an example, in the D_{2h} case, $(\Delta_{41}, \Delta_{42})$ belong to in the two-dimensional representation E_u are separated into one-dimensional representations B_{2u} and B_{3u}, respectively. Similarly, for D'_{2h} case, the linear combination of Δ_{41} and Δ_{42} potential belongs to in one-dimensional representations B_{2u} and B_{3u}. Because D'_{2h} case is the $\pi/4$-rotated version of D_{2h} case, $\Delta_{41} + \Delta_{42}$ $(\Delta_{42} - \Delta_{41})$ is included in B_{3u} (B_{2u}) class when $\Delta_{41} = \Delta_{42}$ $(\Delta_{41} = -\Delta_{42})$. The reclassification of pairing potentials under various lattice distortions is summarized in Table 5.

Superconducting nodal structure. In this subsection, we classify the superconducting nodal structures under lattice distortions and study the symmetry and topology that guarantee the classified nodal structures.

Figure 2 shows the typical nodal structures of superconducting phases of the doped DSM under lattice distortions. There are three types of nodal structures: Full gap, point nodal, and line nodal structures, which are summarized in Table 6. For Δ_1 and Δ'_1 superconducting phases, Δ_1 phase is fully gapped and Δ'_1 phase has two nodal rings regardless of lattice distortions (Fig. 2a–e). For Δ_2 and Δ_3 phases, nodal points exist at the intersections between the k_z axis and the Fermi surfaces in the absence of lattice distortions (Fig. 2a). These points are known to be protected by C_{4z} symmetry[36,37]. Even under lattice distortions, if there is an unbroken mirror symmetry, the topologically protected nodal points can exist and they are protected by the corresponding mirror symmetry (Fig. 2b–e). For Δ_{41} and Δ_{42} phases, there are accidental nodal points at the intersections between the k_z axis and the Fermi surfaces in the absence of lattice distortions (Fig. 2a). However, in the presence of lattice distortions, if there is an unbroken mirror symmetry, there can exist the topologically protected nodal points in the corresponding mirror plane (Fig. 2b–e). Note that all nodal points under lattice distortions in Fig. 2(b–e) are protected by the topological mirror winding numbers, as discussed later.

We now analytically investigate the condition of nodal points in each superconducting phase. Usually, nodal points can exist where the quasi-particle energy spectrum vanishes $\mathscr{E}(\mathbf{k}) = 0$, which gives a set of equations for the momentum variables (k_x, k_y, k_z). If the number of variables N_V is greater than or equal to the number of independent equations N_E, then nodal structures can exist. That is, $N_E \leq N_V = 3$ is the necessary condition for the existence of the nodes. Moreover, if there is mirror symmetry, the necessary condition changes because the number of independent variables is reduced in the corresponding mirror plane. That is, the necessary condition becomes $N_E \leq N_V = 2$. If there is additional mirror symmetry, the necessary condition can be further reduced to $N_E \leq N_V = 1$ on the intersection of two mirror planes.

First, we consider Δ_1 and Δ'_1 superconducting phases. The full gap structure of Δ_1 phase is directly seen from the energy eigenvalues of

$$\mathscr{E}(\mathbf{k}) = \pm\sqrt{(|a| \pm |\mu|)^2 + \langle\Delta_1\rangle^2}, \tag{35}$$

where $|a| = \sqrt{\sum_{i=1}^{5} a_i(\mathbf{k})^2}$. Unless $\langle\Delta_1\rangle = 0$, Δ_1 phase is fully gapped. For Δ'_1 phase, the energy eigenvalues are given by

$$\mathscr{E}(\mathbf{k}) = \pm\sqrt{|a|^2 + \mu^2 + \langle\Delta'_1\rangle^2 \pm 2\sqrt{\mu^2|a|^2 + \langle\Delta'_1\rangle^2\left(|a|^2 - a_5(\mathbf{k})^2\right)}}. \tag{36}$$

From $\mathscr{E}(\mathbf{k}) = 0$, one can obtain the following equations:

$$|a|^2 = \mu^2 + \langle\Delta'_1\rangle^2, \quad a_5(\mathbf{k}) = 0. \tag{37}$$

Because the number of variable $(N_V = 3)$ is larger than the number of equation $(N_E = 2)$, a one-dimensional solution can exist, which leads to the nodal lines. Because this argument works regardless of the lattice distortions, the nodal rings can exist for all cases in Fig. 2. On the other hand, under some lattice distortions, a mixture of Δ_1 and Δ'_1 phases is allowed when Δ_1 and Δ'_1 are in the same representation as shown in Table 5. In such case,

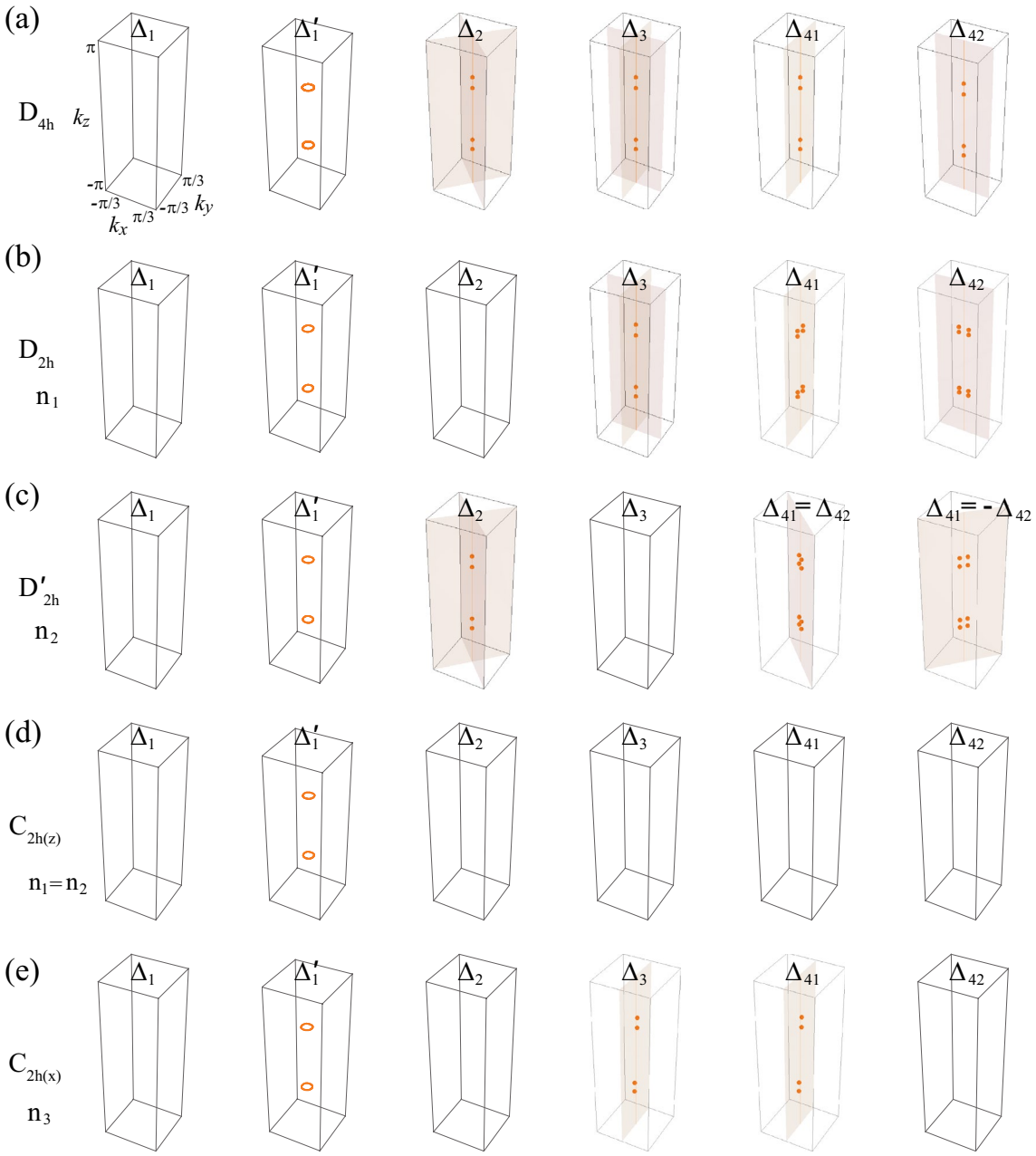

Figure 2. Superconducting nodal structures for pairing potentials under lattice distortions. Nodal structures for **(a)** D_{4h}, **(b)** D_{2h}, **(c)** D'_{2h}, **(d)** $C_{2h(z)}$, and **(e)** $C_{2h(x)}$ cases. The orange point, line, and plane indicate nodal point and nodal line, and mirror plane (M_{xz}, M_{yz}, M_{110}, and $M_{1\bar{1}0}$), respectively. In (**a**–**e**), the Δ_1 phases are fully gapped and the Δ'_1 phases have two nodal rings. In (**a**–**c**, **e**), nodal points are located in the corresponding mirror planes. In (**c**), $\Delta_{42}+\Delta_{41}$ and $\Delta_{42}-\Delta_{41}$ phases are considered instead of Δ_{41} and Δ_{41} phases. In (**d**), the system has no mirror symmetries and hence no nodal points. These nodal structures are summarized in Table 6.

the gap structures have full gap (nodal lines) when $|\langle\Delta_1\rangle| > \left|\langle\Delta'_1\rangle\right|$ ($|\langle\Delta_1\rangle| < \left|\langle\Delta'_1\rangle\right|$) (Fig. S2). See the detailed calculation in Sec. S3 in Supplementary Information.

Next, consider the Δ_2 and Δ_3 superconducting phases. In the absence of lattice distortions, the nodal points in Δ_2 and Δ_3 phases are protected by C_{4z} symmetry[36,37]. On the other hand, under lattice distortions, a mirror symmetry can protect the nodal points that appear in Fig. 2b, c, e. For Δ_3 phase, the energy eigenvalues are given by

$$\mathscr{E}(\mathbf{k}) = \pm\sqrt{|a|^2+\mu^2+\langle\Delta_3\rangle^2 \pm 2\sqrt{\mu^2|a|^2+(a_3(\mathbf{k})^2+a_5(\mathbf{k})^2)\langle\Delta_3\rangle^2}}. \tag{38}$$

From $\mathscr{E}(\mathbf{k})=0$, we get the following equations:

$$|a|^2=\mu^2+\langle\Delta_3\rangle^2, \quad a_1(\mathbf{k})=a_2(\mathbf{k})=a_4(\mathbf{k})=0. \tag{39}$$

	Δ_1	Δ_1'	Δ_2	Δ_3	Δ_{41}	Δ_{42}
D_{4h}	FG	LN [a]	PN [b,c,d]	PN [b,c,d]	Acc. [f]	Acc. [f]
D_{2h}	FG	LN [a]	FG	PN [c,d]	PN [c,e]	PN [c,e]
D_{2h}'	FG	LN [a]	PN [c,d]	FG	PN [c,e]	PN [c,e]
$C_{2h(z)}$	FG	LN [a]	FG	FG	FG	FG
$C_{2h(x)}$	FG	LN [a]	FG	PN [c,e]	PN [c,e]	FG

Table 6. Nodal structures of superconducting phases under lattice distortions. FG, LN, and PN denote full gap, line node, and point node, respectively. [a] Topological line node protected by the chiral winding number ($W = \pm 2$ for each line node). [b] Node protected by C_{4z} symmetry. [c] Topological point node protected by the mirror chiral winding number ($W_M = \pm 2$ for each point node). [d] The nodal point is located on the k_z axis. [e] The nodal point is off the k_z axis. [f] Accidental point node.

Because $N_E = 4$ is larger than $N_V = 3$, there seems to be no allowed nodal point. However, mirror symmetries can allow nodal points. For example, consider D_{2h} point group with M_{yz} and M_{xz} mirror symmetries. Under the M_{yz} mirror operation, $a_1(\mathbf{k})$ and $a_4(\mathbf{k})$ are odd according to Table 2, which gives $a_1(\mathbf{k}) = a_4(\mathbf{k}) = 0$ at the mirror plane $(0, k_y, k_z)$. Similarly, M_{xz} mirror symmetry gives $a_2(\mathbf{k}) = a_4(\mathbf{k}) = 0$ at the mirror plane $(k_x, 0, k_z)$. Thus, along the k_z axis, $a_1(\mathbf{k}) = a_2(\mathbf{k}) = a_4(\mathbf{k}) = 0$ and Eq. (39) is reduced to

$$a_3^2(k_z) + a_5^2(k_z) = \mu^2 + \langle \Delta_3 \rangle^2. \tag{40}$$

Because $N_E = 1$ is equal to $N_V = 1$, nodal points can exist as shown in Fig. 2b. However, when M_{yz} and M_{xz} mirror symmetries are broken, the nodal points for the Δ_3 phase are not protected as shown in Fig. 2c, d.

Similarly, the nodal points in Δ_2 phase can be understood using M_{110} and $M_{1\bar{1}0}$ mirror symmetries. These mirror symmetries allow nodal points on the k_z axis in Fig. 2c. On the other hand, when M_{110} and $M_{1\bar{1}0}$ mirror symmetries are broken, the nodal points disappear as shown in Fig. 2b, d. For the $C_{2h(z)}$ case, a mixture of Δ_2 and Δ_3 phases is possible because Δ_2 and Δ_3 are included in the same A_u representation. However, there is no allowed nodal point as shown in Fig. 2d because there is no helpful mirror symmetry. See the details in Sec. S3 in Supplementary Information.

Finally, consider Δ_{41} and Δ_{42} phases. Without lattice distortions, there are accidental nodal points on the k_z axis (Fig. 2a). The existence of such nodal point is easily seen using four mirror symmetries M_{xz}, M_{yz}, M_{110}, and $M_{1\bar{1}0}$. These mirror symmetries force $a_i(\mathbf{k}) = 0$ for $i = 1, \cdots, 4$ on the k_z axis according to Table 2. Then, the equations for nodal points are given by

$$|a_5(k_z)|^2 = \mu^2 + \langle \Delta_{41} \rangle^2 + \langle \Delta_{42} \rangle^2. \tag{41}$$

Because $N_E = N_V = 1$, the nodal points exist. Because the Δ_{41} and Δ_{42} pairing potentials included in E_u representation of D_{4h} point symmetry group, they break the D_{4h} symmetry spontaneously to D_{2h}. Hence, some of non-zero $a_i(\mathbf{k})$ $(i = 1 \cdots 4)$ are spontaneously generated and the corresponding conditions are introduced, which makes the nodal points vanish. Thus, these nodal points are accidental. However, under lattice distortions, the nodal points can be protected by the unbroken mirror symmetry. For example, when the point group is D_{2h} under the n_1 type lattice distortion, Δ_{41} and Δ_{42} are included in the different representations and thus we can consider each phase separately. For Δ_{41} phase, $a_1(\mathbf{k}) = a_4(\mathbf{k}) = 0$ on the mirror plane $(0, k_y, k_z)$ due to M_{yz} symmetry. Then, the equations for nodes are given by

$$a_2^2(0, k_y, k_z) + a_5^2(0, k_y, k_z) = \mu^2 + \langle \Delta_{41} \rangle^2, \quad a_3(0, k_y, k_z) = 0. \tag{42}$$

Because $N_E = N_V = 2$, there can exist nodal points (Fig. 2b). For Δ_{42} phase, nodal points also can exist due to M_{xz} mirror symmetry (Fig. 2b). When the point group is $D_{2h'}$ under the n_2 type lattice distortion, nodal points can exist due to M_{110} or $M_{1\bar{1}0}$ mirror symmetries (Fig. 2c). For $C_{2h(z)}$, a mixture of Δ_{41} and Δ_{42} phases is possible. However, there is no allowed nodal point due to the lack of mirror symmetry (Fig. 2d). When the point group is $C_{2h(x)}$ under the n_3 type lattice distortion, nodal points can exist due to M_{yz} mirror symmetry (Fig. 2e). See the detailed calculations in Sec. S3 in Supplementary Information.

Stability of nodal structures. There are two types of nodes in Table 6, which are symmetry-protected node and topologically-protected node. In this subsection, we investigate the stability of them.

Chiral winding number. Because of the chiral symmetry of the BdG Hamiltonian, the nodal lines can be protected by a chiral winding number[4,59,60]. The chiral winding number is defined along a path $\mathscr{C}$ enclosing a singular point in the Brillouin zone as shown in Fig. 3a:

$$W = \frac{1}{4\pi i} \oint_{\mathscr{C}} \mathrm{Tr}\left[\Gamma \mathscr{H}^{-1}(\mathbf{k}) d\mathscr{H}(\mathbf{k})\right], \tag{43}$$

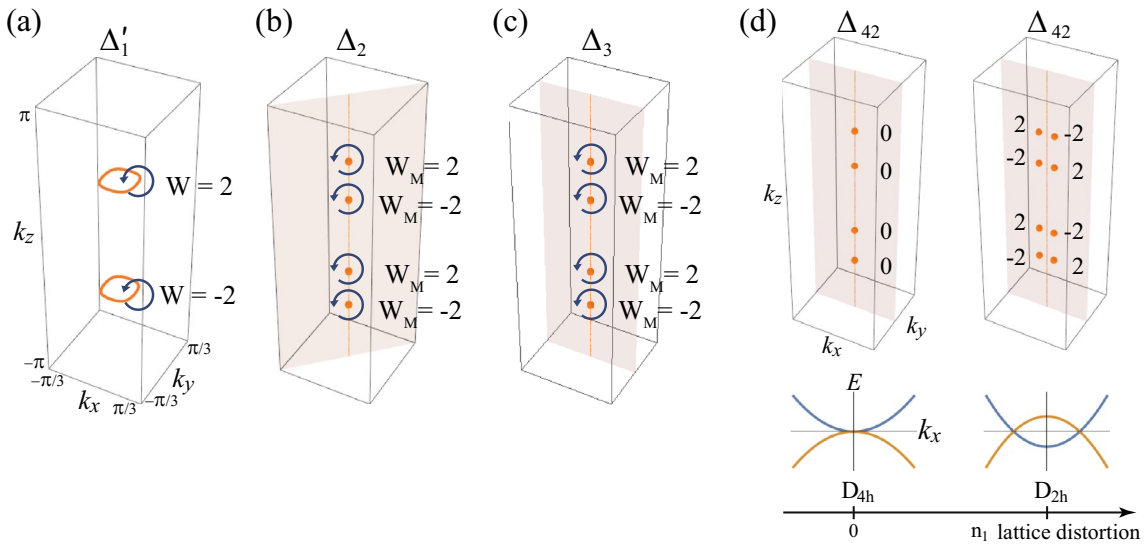

Figure 3. Topologically protected nodal structures and chiral winding numbers. The orange ring, point, plane, and vertical line indicate nodal ring, nodal point, mirror plane, and k_z axis, respectively. Each winding number is defined along each blue loop. **(a)** The chiral winding numbers ($W = \pm 2$) protect nodal rings. **(b, c)** The mirror chiral winding numbers ($W_M = \pm 2$) protect nodal points on the mirror planes. **(d)** Evolution of nodal points in Δ_{42} phases and the corresponding mirror chiral winding number under the n_1 type lattice distortion. For clarity, the blue winding loops are omitted. For $n_1 = 0$, nodal points with $W_M = 0$ are located on k_z axis. These are fine-tuned accidental nodal points because D_{4h} is spontaneously broken into D_{2h} due to Δ_{42} pairing [see the main text below Eq. (41)]. As n_1 increases, the nodal points split into two nodal points with $W_M = \pm 2$. The bottom plot shows the evolution of the energy dispersion along k_x axis. As n_1 increases, the blue (orange) band moves downward (upward), which results in two Dirac points.

where Γ is the chiral operator. As shown in Sec. S4 in Supplementary Information, the transformation property of the winding number under PT symmetry is given by

$$W = -\eta_{\Gamma,\tilde{P}T} W, \tag{44}$$

where the parity $\eta_{A,B} = \pm 1$ is determined by the relation $AB = \eta_{A,B} BA$. For the inversion-even-parity (inversion-odd-parity) pairing potential, $\eta_{\Gamma,\tilde{P}T}$ is -1 ($+1$). Thus, the chiral winding number is zero for the inversion-odd-parity superconductor and only the inversion-even-parity superconducting phases having Δ_1 and Δ_1' pairing potentials can have a nontrivial chiral winding number.

Δ_1 and Δ_1' phases. Because Δ_1 phase is fully gapped, the chiral winding number is zero. On the other hand, two nodal rings in Δ_1' phase are topologically protected by the chiral winding numbers. The calculated chiral winding numbers around the nodal rings are $W = \pm 2$ (Fig. 3). These chiral winding numbers do not change even under the lattice distortions because chiral winding number depends only on T, C, P, and Γ symmetries. Thus, the topologically-protected nodal rings in Δ_1' phase exist regardless of the lattice distortion (Fig. 2).

Mirror chiral winding number. If there is mirror symmetry, the BdG Hamiltonian commutes with the mirror symmetry operator in the mirror plane:

$$[\tilde{M}, \mathscr{H}(\mathbf{k}_M)] = 0. \tag{45}$$

where $\tilde{M}$ is a mirror operator and $\mathbf{k}_M$ is the momentum vector located in the mirror plane. Then, the BdG Hamiltonian can be block-diagonalized according to the mirror eigenvalues $\lambda = \pm i$. Besides, if the mirror operator commutes with the chiral operator,

$$[\Gamma, \tilde{M}] = 0, \tag{46}$$

the chiral operator also can be block diagonalized according to the same mirror eigenvalue. Then, the winding number W_λ in each mirror eigenvalue sector can be defined. The condition in Eq. (46) is satisfied only when the pairing potential is mirror even. The reason is as follows: In our convention, the mirror operator for BdG Hamiltonian is defined as $\tilde{M} = \mathrm{diag}[M, \eta_M s_y M^* s_y]$ where M and $s_y M^* s_y$ are mirror operators for electron part and hole part, respectively. $\eta_M = \pm 1$ is the mirror parity of a pairing potential, which is given in Table 4. Because the mirror operator commutes with the time-reversal operator $[T, M] = 0$, all the mirror operator satisfies $s_y M^* s_y = M$. Then, $\tilde{M} = M\tau_0$ ($\tilde{M} = M\tau_z$) for the mirror-even-parity (mirror-odd-parity) pairing potential. Thus, only the mirror-even-parity superconducting phase satisfies the condition of Eq. (46).

Furthermore, the mirror chiral winding number can be defined as $W_M = W_i - W_{-i}$, where W_λ is the chiral winding number for each block having a mirror eigenvalue λ. The mirror chiral winding number W_M can also be defined for a path $\mathscr{C}$ that encloses the Dirac point in the mirror plane as shown in Fig. 3b. When the path $\mathscr{C}$ is parametrized by $\theta \in [0, 2\pi)$, the mirror chiral winding number is given by[37,61]

$$W_M = \frac{-1}{4\pi} \oint_{\mathscr{C}} d\theta \mathrm{Tr}\left[\tilde{M}\Gamma \mathscr{H}^{-1}(\mathbf{k}(\theta)) d\mathscr{H}(\mathbf{k}(\theta))\right]. \tag{47}$$

Δ_2 and Δ_3 phases. In the absence of lattice distortions, the C_{4z} symmetry protects the nodal points by assigning different eigenvalues[36,37]. The same nodal points are also topologically protected by the mirror chiral winding number in Eq.(47) because the Δ_2 and Δ_3 pairing potentials are mirror-even. For Δ_3 pairing potential, which is mirror-even under M_{xz} and M_{yz}, the calculated mirror chiral winding numbers around the nodal points are ± 2 (Fig. 3c). Similarly, the nodal points in the Δ_2 phase are topologically protected by M_{110} and $M_{1\bar{1}0}$ mirror chiral winding numbers.

Even though C_{4z} symmetry is broken under lattice distortions, the mirror chiral winding number topologically protects the nodal points if the corresponding mirror symmetry is unbroken. For example, consider D_{2h} point group which has M_{xz} and M_{yz} mirror symmetries. Among Δ_2 and Δ_3 pairings, Δ_3 pairing is mirror even under M_{xz} and M_{yz}. Thus, the nodal points in the Δ_3 phase are topologically protected by the corresponding mirror chiral winding numbers (Fig. 3c).

Furthermore, the nodal points are positioned on the k_z axis because C_{2z} symmetry gives an additional constraint as follows: Let $W_M(\mathbf{k})$ denote a mirror chiral winding number at $\mathbf{k}$. Then, the mirror chiral winding number at $C_{2z}\mathbf{k}$ is related with that at $\mathbf{k}$ by

$$W_M(C_{2z}\mathbf{k}) = \eta_{C_{2z}} W_M(\mathbf{k}), \tag{48}$$

where $\eta_{C_{2z}}$ is the parity of the pairing potential under C_{2z} transformation. The detail derivation is in Sec. S4 in Supplementary Information. Since $\eta_{C_{2z}} = 1$ for Δ_2 and Δ_3, $W_M(\mathbf{k}) = W_M(C_{2z}\mathbf{k})$, which means that the mirror chiral winding numbers are the same for the two nodal points that are related by C_{2z} rotation. Now, let us assume that a nodal point on the k_z axis in the absence of lattice distortions deviates from the k_z axis under the n_2 type lattice distortion. Due to the C_{2z} symmetry, there exists another nodal point having the same mirror chiral winding number. Thus, the total mirror winding number under lattice distortion becomes twice the original winding number, which is a contraction with the topological charge conservation. Therefore, the nodal points should be located on the k_z axis under the n_2 type lattice distortion.

A similar argument can be applied to the D'_{2h} case having M_{110} and $M_{1\bar{1}0}$ mirror symmetries. The nodal points in the Δ_2 phase is topologically protected by the M_{110} and $M_{1\bar{1}0}$ mirror chiral winding numbers and the nodal points are located on the k_z axis due to the C_{2z} symmetry (Figs. 2c and 3b). For $C_{2h(x)}$ case, M_{yz} is unbroken while C_{2z} is broken. Thus, nodal points on M_{yz} plane in Δ_3 phase are protected by the M_{yz} mirror chiral winding number and can be deviated from k_z axis due to the C_{2z} symmetry breaking (Fig. 2e).

Δ_{41} and Δ_{42} phases. In the absence of lattice distortions, the nodal points in each Δ_{41} and Δ_{42} phases (Fig. 2a) are accidental nodal points because a single phase, either Δ_{41} or Δ_{42} phase, would break the D_{4h} point group symmetry spontaneously. Only if we neglect such lattice symmetry breaking, the accidental nodal points can be understood to be protected by the different eigenvalues of C_{2z} and s_z symmetry operators (see the details in Sec. S3 in Supplementary Information). Note that the existence of the accidental point nodes also can be verified via C_{4z} symmetry[36,37]. In the viewpoint of topological winding numbers, the mirror chiral winding numbers are zero in the absence of lattice distortions (Fig. 3d) . Due to the C_{2z} symmetry, Eq. (48) gives

$$W_M(0, 0, k_z) = -W_M(0, 0, k_z), \tag{49}$$

which implies that $W_M = 0$ on the k_z axis. Here, $\eta_{C_{2z}} = -1$ is used for Δ_{41} and Δ_{42}. Thus, the nodal points are not topologically protected for D_{4h} case.

However, under lattice distortions, nodal points can be topologically protected by the mirror chiral winding number. Let us consider the D_{2h} point group under the n_1 type lattice distortion. Since Δ_{41} and Δ_{42} pairings are mirror-even under M_{yz} and M_{xz} operations, the corresponding mirror chiral winding number protects nodal points in each mirror plane (Fig. 2b). The calculated mirror chiral winding numbers are $W_M = \pm 2$ (Fig. 3d). Note that the nodal points are off the k_z axis and the calculated mirror chiral winding numbers satisfy Eq. (49). For the D'_{2h} case, M_{110} and $M_{1\bar{1}0}$ mirror chiral winding numbers ($W_M = \pm 2$) protect nodal points in corresponding mirror planes for the superconducting phases having $\Delta_{41} \pm \Delta_{42}$ pairing potentials (Fig. 2c). For the $C_{2h(z)}$ case, all the relevant mirror symmetries are broken and hence there are no topologically-protected nodal points (Fig. 2d). For the $C_{2h(x)}$ case, there are unbroken M_{yz} and C_{2x}. Thus, M_{yz} mirror chiral winding numbers ($W_M = \pm 2$) protect the nodal points but the nodal points need not to be located symmetrically with respect to the k_z axis (Fig. 2e). These nodal points in the $C_{2h(x)}$ case can be understood from the nodal points in the D_{2h} case: Among four nodal points in the D_{2h} case, two nodal points are pair-annihilated, and only two nodal points survive in the $C_{2h(x)}$ case.

Finally, we discuss a gap structure change of Δ_{42} phase under n_1 type lattice distortion (Fig. 3d). When $n_1 = 0$, each nodal points has $W_M = 0$ and a quadratic energy-momentum dispersion relation along the k_x. With the increasing lattice distortion, nodal points with $W_M = \pm 2$ are created pairwise from a nodal point with $W_M = 0$, and linear energy-momentum dispersion relation for all three momentum directions appears. Similar gap structure changes occur under the other lattice distortions.

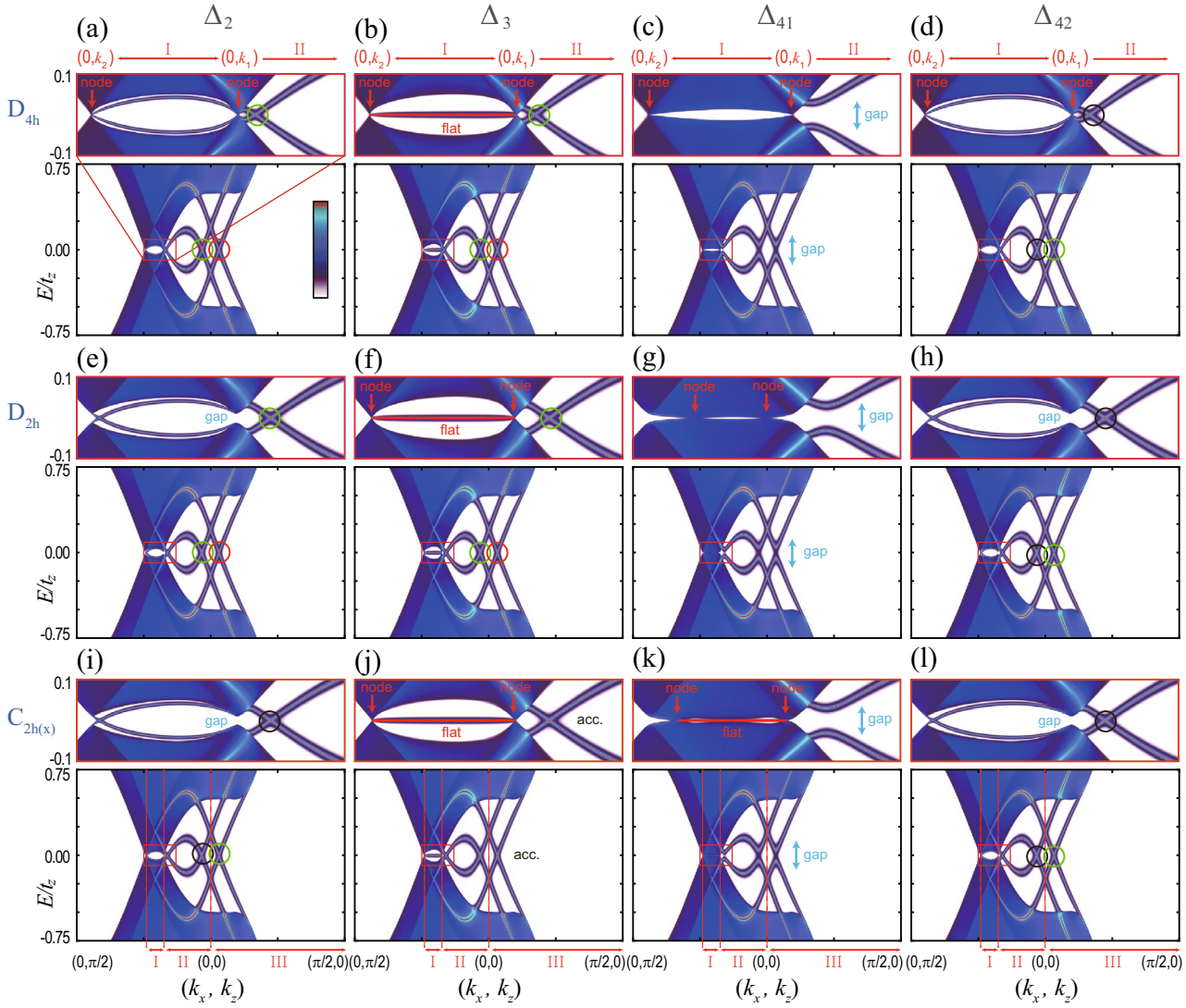

Figure 4. Surface band structures of superconducting phases under distortions. Surface band structures on the (010) surface for (**a**–**d**) D_{4h}, (**e**–**h**) D_{2h}, (**i**–**l**) $C_{2h(z)}$ and (**m**–**p**) $C_{2h(x)}$. In each panel, the upper figure indicates the close-up view of the band structure near $E = 0$ corresponding to the red box in the lower figure. The red vertical arrows indicate the nodal points of the bulk superconducting states. In the insets of (**e**, **h**, **i**, **l**), the bulk states are gapped. The cyan vertical arrows indicate the gapped surface states. In (**b**, **f**, **j**, **k**), red horizontal lines show the surface flat bands. The nature of gapless surface state (GSS) is distinguished by the colored circle: Red ones in (**a**, **b**, **e**, **f**), green ones in (**a**, **b**, **d**–**f**, **h**, **i**, **l**), and black ones in (**d**, **h**, **i**, **l**) indicate GSS's protected by mirror Chern numbers, zero-dimensional topological numbers, and mirror eigenvalues, respectively. In (**j**), GSS's are accidental. The details are in Table 7 and in the main text. Region I, II, and III are $(0, k_1)$– $(0, k_2)$, $(k_2, 0)$– $(0, 0)$, $(0, 0) - (\pi/2, 0)$, respectively, where k_1 and k_2 $(k_1 > k_2 > 0)$ indicate two intersecting points between the upper Fermi surface and the k_z axis.

Surface spectrum. Surface Andreev bound state (SABS) in superconducting phases of the topological DSM have been studied in the absence of lattice distortion[37]. In this subsection, we systematically investigate SABS in superconducting phases under lattice distortions. There are four types of gapless surface Majorana states under lattice distortions. Three types are topologically protected by mirror chiral winding, mirror Chern, and zero-dimensional winding numbers. The fourth type is protected by mirror symmetry and corresponding eigenvalues.

Using the Möbius transformation based method[62], we calculate the surface band structures. Figure 4 shows the numerically obtained surface spectra for (010) surface in various superconducting phases under lattice distortions. For Δ_1 and Δ_1' phases, there is no SABS; Δ_1 phase is fully gapped and topologically trivial, and Δ_1' phase has two nodal lines having opposite chiral winding numbers as shown in Fig. 3a, which does not have protected SABS because of the positions and shapes of two nodes in momentum space. On the other hand, Δ_2, Δ_3, Δ_{41}, and Δ_{42} have various types of SABS (Fig. 4), which are summarized in Table 7.

Pairing	Δ_2			Δ_3			Δ_{41}			Δ_{42}		
Region	I	II	III	I	II	III	I	II	III	I	II	III
D_{4h}	M_{yz}	CM_{xy}	C_M	W_M	CM_{xy}	C_M	n/a	n/a	n/a	M_{yz}	M_{yz}	ΓM_{yz}
D_{2h}	M_{yz}	CM_{xy}	C_M	W_M	CM_{xy}	C_M	n/a	n/a	n/a	M_{yz}	M_{yz}	ΓM_{yz}
$C_{2h(x)}$	M_{yz}	M_{yz}	ΓM_{yz}	W_M	Acc.	Acc.	W_M	n/a	Acc.	M_{yz}	M_{yz}	ΓM_{yz}

Table 7. Gapless surface Andreev bound state (SABS) on (010) surface. The entry is either a topological number or a symmetry operator which protects corresponding gapless surface states. Region I, II, and III are defined in Fig. 4. W_M is a mirror chiral winding number that protects the flat SABS between nodal points. C_M is a mirror Chern number that protects the gapless SABS in M_{xy} plane. ΓM_{yz} and CM_{xy} indicate the symmetry operators which protect gapless SABS using the corresponding zero-dimensional topological number. M_{yz} and M_{xy} indicate the symmetry operators which protect the gapless SABS protected by the corresponding mirror eigenvalues. Acc. indicates an accidental gapless state. n/a means that there is no gapless state.

Without loss of generality, we will focus on the (010) surface and the surface Brillouin zone (k_x, k_z). A similar analysis for the (010) surface can be easily applied to the other surfaces such as (100), (110) planes, because the results for the other plane only depend on the mirror symmetries and the transformation properties of the pairing potentials under the unbroken symmetries. For convenience, we consider the surface states in the three regions: Region I, II, and III, which are $(0, k_1)$-$(0, k_2)$, $(k_2, 0)$-$(0, 0)$, $(0, 0)$-$(\pi/2, 0)$, respectively. Here, k_1 and k_2 $(k_1 > k_2 > 0)$ indicate two intersecting points between the upper Fermi surface and the k_z axis.

First, we consider the flat SABS in the Region I, which is topologically protected by the nontrivial mirror chiral winding number in Eq. (47). For example, let us consider Δ_3 phase and M_{yz} mirror symmetry. For D_{4h}, D_{2h}, and $C_{2h(x)}$ cases, M_{yz} mirror is unbroken and Δ_3 has odd parity under M_{yz}, which leads to the opposite mirror chiral winding numbers $(W_M = \pm 2)$ for two nodal points near the upper Fermi sphere as shown in Fig. 3c. Then, there exists a flat SABS on (010) surface as shown in Fig. 4b, f, j. To understand such SABS on (010) surface, the mirror winding number $W_M(k_z)$ along the mirror invariant k_z axis is defined as[37]

$$W_M(k_z) = \frac{-1}{4\pi i}\int_{-\pi}^{\pi} dk_y \mathrm{Tr}\left[\tilde{M}\Gamma\mathscr{H}^{-1}d_{k_y}\mathscr{H}\right], \tag{50}$$

which is nontrivial between nodal points. Therefore, between the nodal points, there exists a flat SABS. Similarly, for Δ_{41} phase, M_{yz} mirror symmetry gives nontrivial mirror chiral winding numbers, which guarantees the existence of the zero-energy flat SABS in the Region I on (010) surface (Fig. 4k). Note that, under the n_3 type lattice distortion, the mixture of Δ_3 and Δ_{41} phases are allowed. But the flat SABS is still present due to the M_{yz} mirror chiral winding number.

Second, we consider the gapless SABS protected by the mirror Chern number C_M. The topological mirror superconducting phases[36,63] are allowed for Δ_2 and Δ_3 phases because Δ_2 and Δ_3 pairing potentials are M_{xy} mirror-odd and the corresponding mirror Chern numbers for each mirror eigenvalue block are nontrivial. Under the n_1 (n_2) type lattice distortion, Δ_2 (Δ_3) phase is fully gapped, and the mirror Chern number defined in M_{xy} plane is nontrivial $(C_M = \pm 2)$, which leads to a topologically-protected Majorana states on M_{xy} plane. For example, see the surface spectra in the Region III in Fig. 4e.

Third, we consider the gapless SABS protected by the zero-dimensional topological number. Since Δ_2 and Δ_{42} pairings are odd under M_{yz}, a zero-dimensional topological number $\rho(k_x)$ can be defined using ΓM_{yz}[36,37]. Then, the zero-dimensional topological number protects the gapless state in the Region III. See the surface spectra at the Region III in Fig. 4d, h, i, l and Table 7. Similarly, Δ_2 and Δ_3 pairings are odd under M_{yz}, a zero-dimensional topological number $\rho(k_z)$ is defined using CM_{yz}[36,37], which protects the gapless states in the Region II for D_{4h} and D_{2h} cases. See the surface spectra at the Region II in Fig. 4a, b, e, f and Table 7.

Fourth, we consider the gapless SABS protected by mirror eigenvalues. If the pairing potential has an odd parity under the mirror operation, the mirror eigenvalues for the electron and hole bands are different, which protects the band crossing of surface states[36,37]. For example, consider Δ_2 phase and M_{yz} symmetry. Because $(k_x, k_y, k_z) \to (-k_x, k_y, k_z)$ under M_{yz}, the mirror eigenvalues are properly defined on the k_z axis. Moreover, Δ_2 pairing has odd parity under M_{yz} symmetry. Hence, the different mirror eigenvalues protect the gapless states in the Region I. See Fig. 4a, e, i. Similarly, Δ_{42} phases has odd parity under M_{yz}, which protects the gapless states in the Region I and II. See Fig. 4d, h, l.

In summary, we find the various types of surface states depending on the pairing potentials and lattice distortions. Even under the lattice distortions, most of the inversion-odd-parity superconducting phases have gapless SABS, which may be observed as zero bias conductance peak (ZBCP) in experiments.

Superconducting critical temperature and phase diagram. In this subsection, we study superconducting critical temperatures and their enhancements under lattice distortions. We also investigate the phase diagram for the various superconducting phases under lattice distortion.

In the weak-coupling limit, the superconducting critical temperature T_c can be calculated by solving the linearized gap equation and a phase diagram for various pairing potentials is obtained by comparing the critical temperatures[37,55–58]. The linearized gap equation can be expressed using the pairing susceptibility[37,55–58]. The pairing susceptibility χ_i for each pairing potential Δ_i is given by

$$\chi_i(T) = -\frac{1}{\beta}\sum_{\omega_n}\sum_{\mathbf{k}} \mathrm{Tr}[(\Delta_i\tau_x)G_0(\mathbf{k})(\Delta_i\tau_x)G_0(\mathbf{k})]. \tag{51}$$

Here, $\beta = 1/(k_B T)$ is the inverse temperature, k_B is the Boltzmann constant, ω_n is the Matsubara frequency, and Δ_i is the matrix representation of a pairing potential listed in Table 4. $G_0(\mathbf{k}) = \frac{\mathscr{P}_{\mathbf{k}}}{i\omega_n - \varepsilon_{\mathbf{k}}}$ is the single-particle Green's function of the normal state and $\mathscr{P}_{\mathbf{k}} \equiv \sum_{m=1,2} |\phi_{m,\mathbf{k}}\rangle\langle\phi_{m,\mathbf{k}}|$ is the projection operator onto the two degenerate Bloch states in the conduction bands. Here, $\varepsilon_{\mathbf{k}} = |a(\mathbf{k})| - \mu$. Then, the superconducting susceptibility has the following generic form:

$$\chi_i(T) = \int \frac{d^3\mathbf{k}}{(2\pi)^3} f_i(\mathbf{k}) \frac{\tanh(\beta\varepsilon_{\mathbf{k}}/2)}{2\varepsilon_{\mathbf{k}}}, \tag{52}$$

where $f_i(\mathbf{k})$ is momentum dependent form factor. The explicit expressions for form factors $f_i(\mathbf{k})$ are given in Sec. S5 in Supplementary Information.

With these susceptibilities, we now solve the linearized gap equation. The linearized gap equations are obtained by minimizing the mean-field free energy in the weak coupling limit. Since superconducting critical temperatures with pairing potentials in the same classes are not independent, the Δ_i's in the same class can appear in the same linearized gap equation.

First, consider the gap equation in the absence of lattice distortions. According to the irreducible representation of D_{4h}, Δ_1's, Δ_2, Δ_3 and Δ_4's belong to A_{1g}, B_{1u}, B_{2u} and E_u irreducible representations (see Table 5). Then, the gap equations are given by

$$\begin{vmatrix} U\chi_1(T_c) - 1 & U\chi_{1,1'}(T_c) \\ U\chi_{1,1'}(T_c) & U\chi_{1'}(T_c) - 1 \end{vmatrix} = 0, \quad \text{for } \Delta_1 \text{ and } \Delta_1' \text{ phases}, \tag{53}$$

$$V\chi_2(T_c) - 1 = 0, \quad V\chi_3(T_c) - 1 = 0, \quad \text{for } \Delta_2 \text{ and } \Delta_3 \text{ phases}, \tag{54}$$

$$\begin{vmatrix} V\chi_{41}(T_c) - 1 & V\chi_{41,42}(T_c) \\ V\chi_{41,42}(T_c) & V\chi_{42}(T_c) - 1 \end{vmatrix} = 0, \quad \text{for } \Delta_{41} \text{ and } \Delta_{42} \text{ phases}, \tag{55}$$

where $\chi_{i,j}$ is the generalized superconducting susceptibility for mixed pairings Δ_i and Δ_j by replacing the second Δ_i with Δ_j in Eq. (51). Using the low-energy effective Hamiltonian in Eq. (13), the superconducting susceptibility can be further simplified and hence one can solve the gap equation analytically. Using an ellipsoidal coordinate, the superconducting susceptibility can be represented as a product of two independent integrals (see more details in Sec. S5 in Supplementary Information):

$$\chi_i = \mathscr{R}(\beta_c)\Omega_i(\mu). \tag{56}$$

Here, the radial integral part $\mathscr{R}(\beta_c)$ is given by

$$\mathscr{R}(\beta_c) = \int_{-\omega_D}^{\omega_D} dE \, \frac{\tanh(\beta_c E/2)}{E}, \tag{57}$$

where E is an integration variable and ω_D is the energy cutoff of the pairing potential. The angular integral part $\Omega_i(\mu)$ is given by

$$\Omega_i(\mu) = \int_0^{\pi}\int_0^{2\pi} \frac{d\theta d\phi}{(2\pi)^3} \left|\frac{2\mu^2 \sin\theta}{v^2 v_z}\right| f_i(r=\mu,\theta,\phi), \tag{58}$$

where the form factor $f_i(\mathbf{k})$ is represented as a function of r, θ and ϕ in the ellipsoidal coordinates. After the integration over θ and ϕ, the susceptibilities can be obtained as follows:

$$\chi_1 = 4\pi C_0 \mathscr{R}(T_c), \ \chi_{1'} = \frac{4\pi}{3} C_0 \mathscr{R}(T_c), \ \chi_2 = \chi_3 = \frac{8\pi}{3} C_0 \mathscr{R}(T_c), \ \chi_{41} = \chi_{42} = \frac{4\pi}{3} C_0 \mathscr{R}(T_c), \ \chi_{1,1'} = \chi_{41,42} = 0, \tag{59}$$

where $C_0 = \frac{2}{(2\pi)^3}\frac{\mu^2}{v^2 v_z}$. Then, the linearized gap equations are given by

$$\chi_1(T_c) = \chi_{1'}(T_c) = 1/U, \tag{60}$$

$$\chi_2(T_c) = \chi_3(T_c) = \chi_{41}(T_c) = \chi_{42}(T_c) = 1/V. \tag{61}$$

If we denote the critical temperature $T_c^{(i)}$ for a pairing potential Δ_i, then the gap equations are given by

$$\mathscr{R}(T_c^{(1)}) = \frac{1}{3}\mathscr{R}(T_c^{(1')}) = \frac{1}{4\pi U C_0}, \tag{62}$$

$$\mathscr{R}(T_c^{(2)}) = \mathscr{R}(T_c^{(3)}) = \frac{1}{2}\mathscr{R}(T_c^{(41)}) = \frac{1}{2}\mathscr{R}(T_c^{(42)}) = \frac{3}{8\pi V C_0}. \tag{63}$$

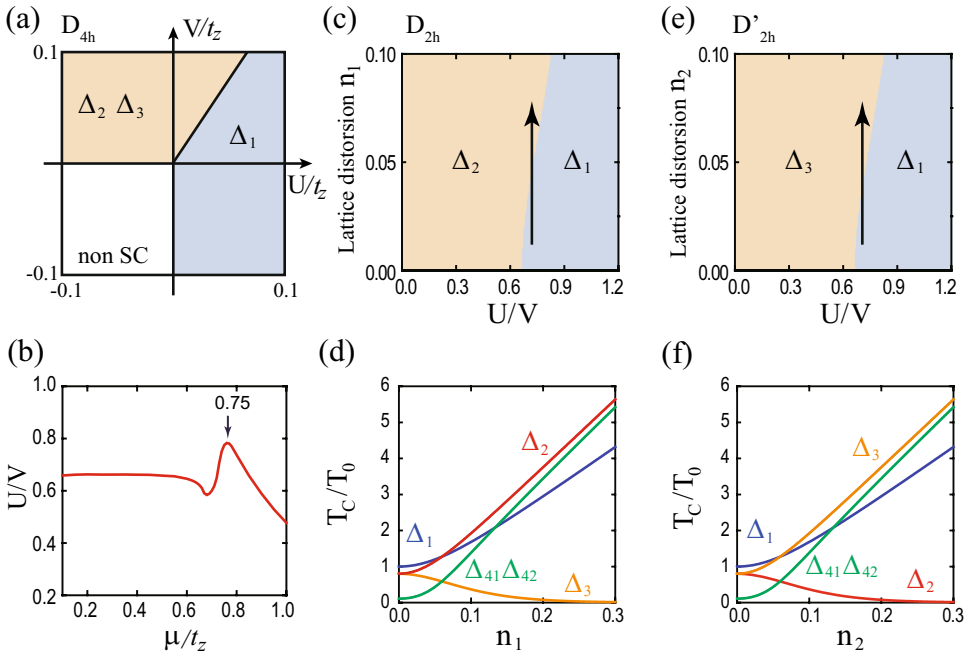

Figure 5. Phase diagrams for the tetragonal and orthorhombic crystal systems. **(a)** Superconducting phase diagram in the U and V plane in the absence of lattice distortions when $\mu/t_z = 0.1$. In the orange (blue) region, Δ_2 or Δ_3 (Δ_1) phase is dominant. The slope of the phase boundary is approximately $U/V = 2/3$. The white region indicates a non-superconducting phase. **(b)** The numerically calculated critical value of U/V ratio as a function of the chemical potential in the absence of lattice distortions. Since $\mu = 0.75t_z$ is the band inversion point, there is a local maximum due to Van Hove singularity near $\mu = 0.75t_z$. **(c, e)** Phase diagrams with respect to (**c**) n_1 and (**e**) n_2 type lattice distortions when $U = 0.045t_z$. The corresponding point groups are (**c**) D_{2h} and (**e**) D'_{2h}. Each black arrow indicates the possible phase transition from an inversion-even-parity to inversion-odd-parity superconducting phases. **(d, f)** The normalized critical temperature T_c/T_0 for various pairing potentials with respect to (**d**) n_1 and (**f**) n_2 type lattice distortions. In both figures, $U/V = 0.75$ and $U = 0.045t_z$, which corresponds to the black arrows in (**c**, **e**). T_0 is the critical temperature of the Δ_1 phase in the absence of the lattice distortions.

Because $\mathscr{R}(x)$ is a monotonically decreasing function with respect to x, $T_c^{(1)} > T_c^{(1')}$ and $T_c^{(2)} = T_c^{(3)} > T_c^{(41)} = T_c^{(42)}$. Thus, the highest T_c is determined among $T_c^{(1)}$, $T_c^{(2)}$ and $T_c^{(3)}$. Because the critical temperatures are same at the phase boundary, the phase boundary in Fig. 5a is determined by the equation $\mathscr{R}(T_c^{(1)}) = \mathscr{R}(T_c^{(2)}) = \mathscr{R}(T_c^{(3)})$, which gives the critical value of $U/V = 2/3$.

When the chemical doping is low, the superconducting phase diagram for undistorted Dirac semimetal is shown in Fig. 5a. When the intra-orbital interaction U is strong, the conventional s-wave superconductivity with pairing potential Δ_1 is the dominant phase. However, with the increasing inter-orbital interaction V, the unconventional superconducting phase with inter-orbital pairing potential Δ_2 or Δ_3 can emerge. Figure 5b shows the numerically obtained critical value of U/V ratio using the lattice Hamiltonian. Thus, by controlling the U/V ratio, both conventional and unconventional superconductivity can emerge for for the large range of chemical doping. The calculated value of U/V ratio is similar with 2/3 using the low-energy effective Hamiltonian, which means that Δ_2 or Δ_3 phase can emerge for the large range of chemical doping.

Next, consider the effect of n_1 and n_2 types of lattice distortions on the superconducting temperatures and the phase diagrams. When n_1 type lattice distortion is turned on, the point group becomes D_{2h}. In this case, only Δ_1 and Δ'_1 belong to the same A_g class, and the others are belong to different classes (see Table 5). So the linearized gap equation is given by

$$\begin{vmatrix} U\chi_1(T_c) - 1 & U\chi_{1,1'}(T_c) \\ U\chi_{1,1'}(T_c) & U\chi_{1'}(T_c) - 1 \end{vmatrix} = 0, \quad \text{for } \Delta_1 \text{ and } \Delta'_1 \text{ phases,} \tag{64}$$

$$V\chi_2(T_c) = V\chi_3(T_c) = V\chi_{41}(T_c) = V\chi_{42}(T_c) = 1, \quad \text{for } \Delta_2, \Delta_3, \Delta_{41}, \text{and } \Delta_{42} \text{ phases.} \tag{65}$$

Similar to D_{4h} case, the susceptibility can be analytically calculated when the chemical doping level is small. The relevant gap equations that determine the phase map are given by

$$\mathscr{R}(T_c^{(1)}) = \frac{1}{4\pi UC_0}, \quad \mathscr{R}(T_c^{(2)}) = \frac{1}{\frac{4\pi}{3}(2 + \frac{n_1^2 \sin^2 k_0}{\mu^2})VC_0}. \tag{66}$$

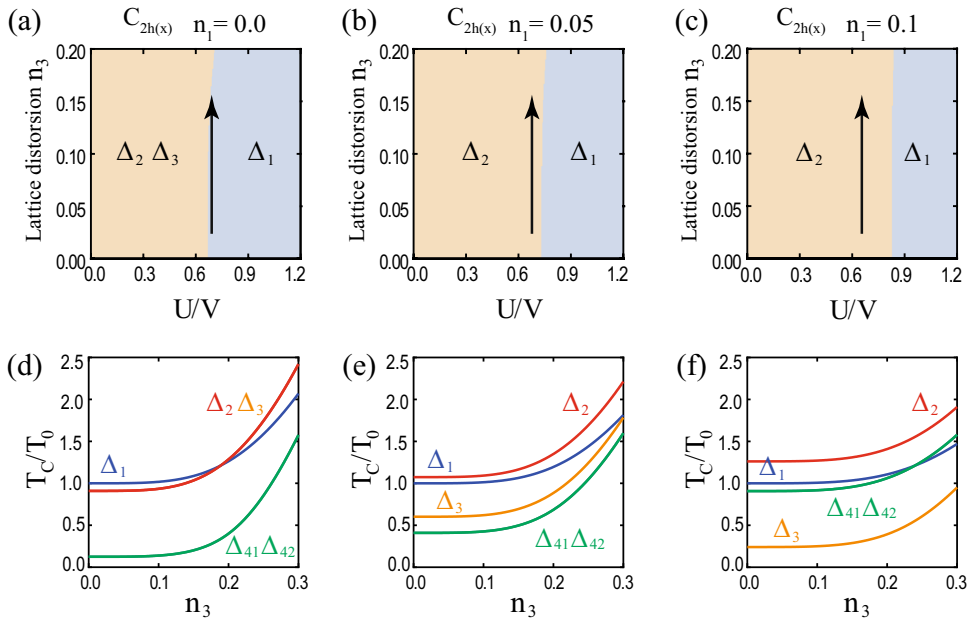

Figure 6. Phase diagrams for the monoclinic crystal system. (**a**–**c**) Phase diagrams with respect to U/V ratio and n_3 type lattice distortions for (**a**) $n_1 = 0.0$, (**b**) $n_1 = 0.05$, and (**c**) $n_1 = 0.1$. (**d**–**f**) The normalized critical temperature T_c/T_0 along the black arrows in (**a**–**c**). Here, $U/V = 0.7$ and T_0 is the critical temperature of the Δ_1 phase in the absence of the lattice distortions. In (**d**), the red and orange lines for Δ_2 and Δ_3 overlap.

Thus, the phase boundary is given by

$$\frac{U}{V} = \frac{2 + (n_1^2 \sin^2 k_0)/\mu^2}{3}. \tag{67}$$

Similarly, the other cases can be calculated. See the details in Supplementary Information.

Figure 5a shows the numerically calculated phase map in the absence of lattice distortions, which is consistent with the previous work[37]. The superconducting phases are separated by the $U/V = 2/3$ line as shown in Fig. 5a and the U/V ratio of the phase boundary depends on the chemical potential as shown in Fig. 5b. However, such superconducting phase is not reported in the real materials of Au_2Pb and Cd_2As_3 in the absence of lattice distortion. Such discrepancy might happen because either Tc is very low or the interaction strength is repulsive in real materials at ambient pressure.

Figure 5c–f shows the numerically calculated phase maps under the n_1 and n_2 types of lattice distortions using the low-energy effective Hamiltonian. The phase diagrams are plotted in the plane of the U/V ratio versus strength of n_1 or n_2 type lattice distortion. In each diagram, the dominant phases are conventional spin-singlet Δ_1 phase and unconventional spin-triplet Δ_2 or Δ_3 phase depending on the parameters. When U/V is small (large) enough, Δ_2 or Δ_3 (Δ_1) phase emerges. Remarkably, the unconventional superconductivity can emerge with increasing lattice distortions. As an example, near the phase boundary of $U/V \approx 0.7$, there is a phase transition between conventional superconducting Δ_1 and unconventional superconducting Δ_2 phases when n_1 increases (see the black arrow in Fig. 5c). To see this phase transition more clearly, we plot the normalized superconducting critical temperatures along the black arrow (Fig. 5d). When $n_1 = 0$, the Δ_1 phase is dominant. With increasing n_1, the superconducting critical temperatures for Δ_2 are increasing, which leads to the Δ_2 superconducting phase under enough lattice distortion. Note that T_c's for Δ_1, Δ_2, Δ_{41}, and Δ_{42} increase while T_c for Δ_3 decreases with the increasing n_1 (Fig. 5d). This can be explained by the expectation values of the Cooper pairings and spin-orbital texture at the Fermi surface, which will be discussed later. Because n_1 and n_2 type lattice distortions are related with $\pi/4$ rotation, similar features are observed except for the exchange of Δ_2 and Δ_3 phases (Fig. 5e, f).

For the n_3 type lattice distortion, similar features can be observed in Fig. 6. Under the n_3 type lattice distortion, n_1 type lattice distortions also can be involved as discussed before. Thus, we plot three representative phase diagrams for $n_1 = 0.0$, 0.05, and 0.1. Surprisingly, when $n_1 = 0$, Δ_2 and Δ_3 phases are degenerate, and they are dominant unconventional phases as shown in Fig. 6a,d. With increasing n_1, the region of the unconventional phase Δ_2 increases (Fig. 6a–c) and the degenerate Δ_2 and Δ_3 phases become distinguishable.

Under n_1, n_2, and n_3 lattice distortions, the T_c's of Δ_2, Δ_3, Δ_{41}, and Δ_{42} increases much more than that of Δ_1 (Figs. 5d, f, 6d–f), and hence the unconventional superconducting phases emerge. The mechanism of this will be discussed below.

Mechanism for T_c enhancement of unconventional superconductivity. The T_c enhancement of unconventional superconductivity under lattice distortions can be understood by the enhancement of DOS at

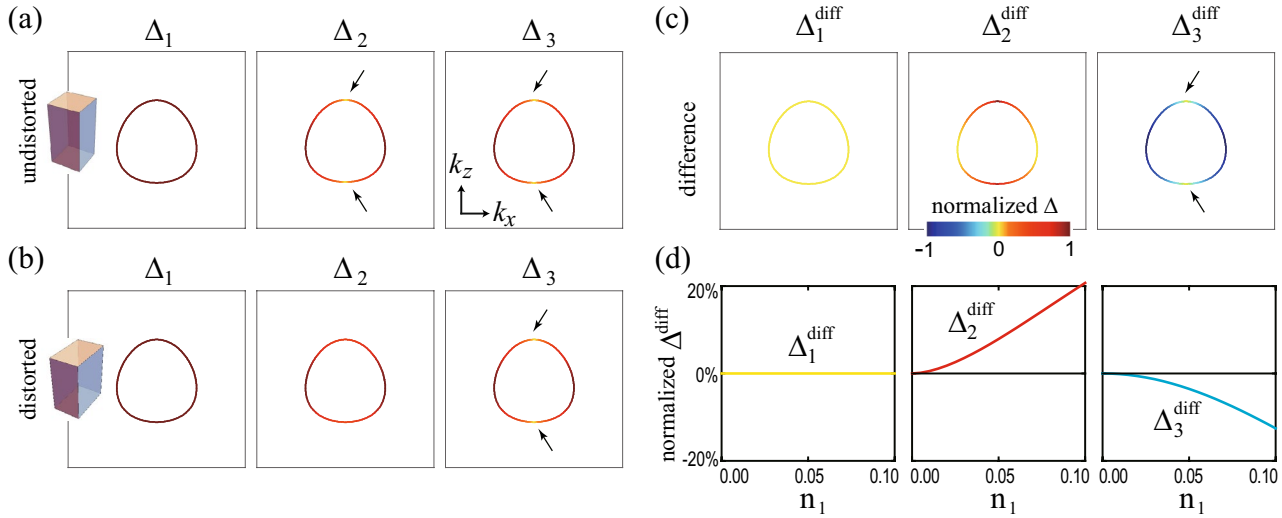

Figure 7. Expectation values of pairing potentials at the upper Fermi surface under the n_1 type lattice distortion. (**a**, **b**) The normalized expectation values $\langle\Delta_i\rangle$ of Δ_1, Δ_2, and Δ_3 (**a**) without and (**b**) with the n_1 type lattice distortion are plotted at the upper Fermi surface of DSM in the k_x-k_z plane. **(c)** The differences $\Delta_i^{\text{diff}} \equiv \langle\Delta_i\rangle_{n_1\neq 0} - \langle\Delta_i\rangle_{n_1=0}$ are plotted. In (**a**–**c**), the black arrows indicate the points having zero expectation values. **(d)** The normalized integrated expectation values of each pairing potentials, $\int_{\text{FS}} d^2k\Delta_i^{\text{diff}} / \int_{\text{FS}} d^2k\langle\Delta_i\rangle_{n_1=0}$, are plotted with respect to n_1. Note that the upper Fermi surfaces encloses the Dirac point $(0, 0, k_0)$ as shown in Fig. 1(**k**–**o**).

Fermi surface and the enhancement of the expectation values of unconventional pairings at Fermi surfaces due to the unique spin-orbital texture.

First, we consider the increment of DOS at the Fermi surface. Under the lattice distortions, the DOS's at the Fermi surface increase as shown in Eqs. (20) and (22). Then, the superconducting critical temperature increases under lattice distortions because $T_c \propto e^{-\frac{1}{gN(0)}}$. Here, g is the strength of the pairing potential in the standard BCS theory and $N(0)$ is the DOS at Fermi surface. Due to this enhancement of DOS, most of the superconducting temperatures increase under the lattice distortions (see Figs. 5d, f and 6d–f). However, some unconventional superconducting temperatures decrease while some unconventional superconducting temperatures increase under lattice distortions. To understand this, we investigate the pairing expectation values for each superconducting pairing potentials.

As a representative example, we calculate the normalized expectation values for the Δ_1, Δ_2, and Δ_3 pairings at the Fermi surface with and without the n_1 type lattice distortion (Fig. 7a, b). For a clear comparison, the differences $\Delta_i^{\text{diff}} \equiv \langle\Delta_i\rangle_{n_1\neq 0} - \langle\Delta_i\rangle_{n_1=0}$ are calculated (Fig. 7c). Without lattice distortions, $\langle\Delta_1\rangle$ is uniform while $\langle\Delta_2\rangle$ and $\langle\Delta_3\rangle$ show zeros on the k_z axis. With the n_1 type lattice distortion, $\langle\Delta_2\rangle$ increases while $\langle\Delta_3\rangle$ decreases, which leads to $\Delta_2^{\text{diff}} > 0$ and $\Delta_3^{\text{diff}} < 0$ (Fig. 7c, d). On the other hand, $\Delta_1^{\text{diff}} = 0$. These behaviors of the expectation values of $\langle\Delta_i\rangle$ explains that the tendency of T_c under lattice distortions. T_c of Δ_2 phase increase greater than that of Δ_1 phase while T_c of Δ_3 phase decreases under n_1 type lattice distortion (Fig. 5a). Similarly, the effect of the other types of lattice distortions on T_c can be understood by the expectation value change of the pairing potentials.

Microscopically, we can understand the emergence of unconventional superconducting phases under lattice distortions as a result of the enhancement of inter-orbital pairing at the Fermi surface. Even though our argument can be applied to all distortions, we discuss the effect of n_1 type lattice distortion for convenience. We consider two Fermi surfaces encapsulating Dirac points $(0, 0, \pm k_0)$ which are related by time-reversal and inversion. On the upper Fermi surface near the Dirac point $(0, 0, +k_0)$, the Dirac Hamiltonian in Eq.(18) in the k_x-k_z plane is given by

$$H_{\text{Dirac}} = (n_1 \sin k_0 s_x + v k_x s_z)\sigma_x + v_z(k_z - k_0)\sigma_z. \tag{68}$$

The spin and orbital parts can be diagonalized separately and the total wavefunction can be represented by the product of spin and orbital wavefunctions[37]:

$$|\Psi\rangle = |\phi\rangle_{\text{orbital}} \otimes |\psi\rangle_{\text{spin}}. \tag{69}$$

Let us diagonalize the spin part. The spin part of Hamiltonian is given by

$$H_{\text{spin}} = (n_1 \sin k_0 s_x + v k_x s_z) = \mathbf{h}\cdot\mathbf{s}, \tag{70}$$

where $\mathbf{h} = (n_1 \sin k_0, 0, v k_x)$. Since this Hamiltonian is a product of momentum and spin operators, the spin wavefunction can be represented in the helicity basis $|\lambda\rangle_{\text{spin}}$ with $\lambda = \pm 1$:

$$H_{\text{spin}}|\lambda\rangle_{\text{spin}} = \lambda|\mathbf{h}||\lambda\rangle_{\text{spin}}. \tag{71}$$

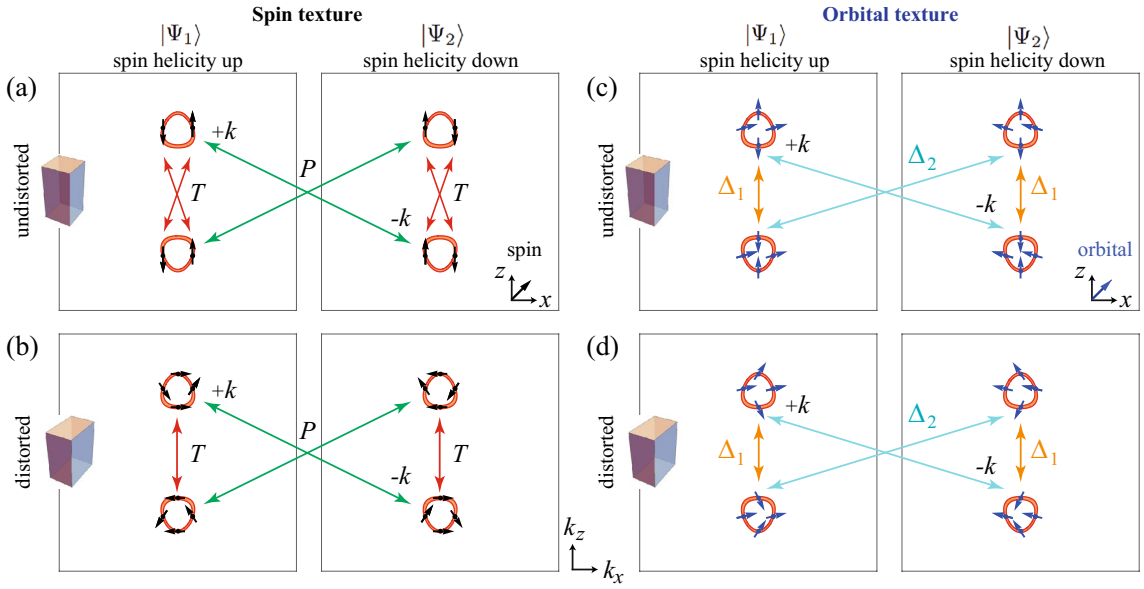

Figure 8. Spin and orbital textures without and with lattice distortion. (**a**, **d**) [(c,d)] Numerically calculated spin (orbital) textures at two Fermi surface surfaces. The n_1 type lattice distortion is absent in (**a**, **c**) and present in (**b**, **d**). In (**a**, **b**) [(c,d)], the spin (orbital) textures are represented by the small black (blue) arrows. In (**a**–**d**), the textures in left and right panels correspond to the spin helicity up and down wavefunctions, respectively. In (**a**, **b**), the red and green arrows indicate time-reversal and inversion pairs, respectively. In (**c**, **d**), the orange and blue arrows indicate the possible Cooper pairing between two electrons with opposite momenta. Note that the orbital pseudo-spin vectors connected by orange arrows are parallel regardless of the lattice distortion. On the other hand, the orbital pseudo-spin vectors connected by cyan arrows are parallel in (**c**) while non-parallel in (**d**).

Next, we diagonalize the remaining orbital part. Depending on the spin helicity λ, the Hamiltonian in Eq. (68) can be written as follows:

$$H_{\text{orbital},\,\lambda} = \lambda|\mathbf{h}|\sigma_x + v_z(k_z - k_0)\sigma_z = \mathbf{d}_\lambda \cdot \boldsymbol{\sigma}, \tag{72}$$

where $\mathbf{d}_\lambda = (\lambda|\mathbf{h}|, 0, d_z)$ and $d_z = v_z(k_z - k_0)$. The orbital wavefunction can be represented by the pseudo-spin along $\hat{\mathbf{d}}_\lambda$. For each spin helicity λ, there are two orbital wavefunctions $\left|\kappa\hat{\mathbf{d}}_\lambda\right\rangle_{\text{orbital}}$ with $\kappa = \pm 1$ that satisfy the following equations:

$$H_{\text{orbital},\,\lambda}\left|\kappa\hat{\mathbf{d}}_\lambda\right\rangle_{\text{orbital}} = \kappa d\left|\kappa\hat{\mathbf{d}}_\lambda\right\rangle_{\text{orbital}}, \tag{73}$$

where $d = \sqrt{|\mathbf{h}|^2 + d_z^2}$. When the chemical potential is positive, two degenerate wavefunctions located in conduction bands participate in the superconducting pairing. These wavefunctions are given by

$$|\Psi_1\rangle = \left|\hat{\mathbf{d}}_+\right\rangle_{\text{orbital}} \otimes |+\rangle_{\text{spin}}, \qquad |\Psi_2\rangle = \left|\hat{\mathbf{d}}_-\right\rangle_{\text{orbital}} \otimes |-\rangle_{\text{spin}}, \tag{74}$$

which form a Kramer's pair due to the PT symmetry regardless of lattice distortions: PT operation conserves the momentum while it flips helicity and the x-component of the orbital because $T = is_y\hat{K}$ and $P = -\sigma_z$.

Since we have obtained the spin and orbital texture in one Fermi surface, we can obtain the spin and orbital texture of the other Fermi surface by applying either time-reversal or inversion operator. Let $\Psi(\mathbf{k})$ be a wavefunction on the Fermi surface. Because there is no σ_y in the Hamiltonian Eq. (68), the time-reversal partner $T\Psi(\mathbf{k})$ has the same orbital direction and the opposite spin direction regardless of lattice distortions comparing with $\Psi(\mathbf{k})$. On the other hand, since $P = -\sigma_z$, the inversion partner $P\Psi(\mathbf{k})$ has the opposite d_x while keeping d_z and spin direction comparing with $\Psi(\mathbf{k})$. Figure 8 shows the numerically calculated spin and orbital textures using the lattice model. The P and T symmetry operators connects spin and orbital wavefunctions in Fig. 8. The red and green arrows indicate time-reversal and inversion pairs, respectively.

Using these spin and orbital textures, let us investigate how the lattice distortions promote the unconventional pairings. The conventional Δ_1 pairing is not affected by the lattice distortion. The expectation value of Δ_1 is constant over the entire Fermi surface regardless of lattice distortion as shown in Fig. 7a, b. Because $\Delta_1 = c^\dagger_{1\uparrow}c^\dagger_{1\downarrow} + c^\dagger_{2\uparrow}c^\dagger_{2\downarrow} + H.c.$ connects two wavefunctions that are related by time-reversal, the expectation value of Δ_1 is constant due to TRS. In other words, because Δ_1 is represented by the identity matrix $1_{4\times4}$, the expectation value of the Δ_1 over the Fermi surface is constant even under the lattice distortions.

On the other hand, n_1 type lattice distortion can increase the expectation values of the inter-orbital pairing Δ_2. For example, let us consider two wavefunctions located at the south pole of the upper Fermi surface ($k_z = +k_s$

Type	Gap	Class	Topological invariant	Classification	Δ's
Line nodal SC	LN	DIII + P_{even}	W	$2\mathbb{Z}$	Δ_1, Δ_1'
Topological mirror SC	FG	DIII + P_{odd} + M_{odd}	C_M	$2\mathbb{Z}$	Δ_2, Δ_3
Point nodal SC	PN	DIII + P_{odd} + M_{even}	W_M	$2\mathbb{Z}$	$\Delta_2, \Delta_3, \Delta_{41}, \Delta_{42}$

Table 8. Possible topological superconductivity in doped DSM under lattice distortions. SC, FG, LN, and PN denote superconductor, full gap, line node, and point node, respectively. P_{odd} and P_{even} represent the inversion-odd and inversion-even parity superconductors. M_{odd} and M_{even} represent the mirror-odd and mirror-even parity superconductors. C_M is the mirror Chern number. W is chiral winding number defined by Eq. (43). W_M is the mirror chiral winding number defined by Eq. (47). Here, the $2\mathbb{Z}$ indicates the even number of the corresponding surface Andreev bound state (SABS).

with $k_s < k_0$) and the north pole of the lower Fermi surface ($k_z = -k_s$). Two wavefunctions are indicated by the orange and cyan arrows in Fig. 8c, d. At $k_z = \pm k_s$, the Dirac Hamiltonian in Eq.(18) is given by

$$H_{\text{Dirac}}^{(\pm)} = \pm n_1 \sin k_0 s_x \sigma_x - v_z(k_0 - k_s)\sigma_z, \tag{75}$$

where $H_{\text{Dirac}}^{(+)}$ and $H_{\text{Dirac}}^{(-)}$ correspond $k_z = k_s$ and $k_z = -k_s$, respectively. When $n_1 = 0$, wave functions on the conduction bands at $k_z = \pm k_s$ are given by

$$|2\rangle_{\text{orbital}} \otimes |\uparrow_x\rangle_{\text{spin}}, \quad |2\rangle_{\text{orbital}} \otimes |\downarrow_x\rangle_{\text{spin}}, \quad \text{for } k_z = +k_s, \tag{76}$$

$$|2\rangle_{\text{orbital}} \otimes |\uparrow_x\rangle_{\text{spin}}, \quad |2\rangle_{\text{orbital}} \otimes |\downarrow_x\rangle_{\text{spin}}, \quad \text{for } k_z = -k_s, \tag{77}$$

where $|1\rangle_{\text{orbital}}$ and $|2\rangle_{\text{orbital}}$ indicate the orbital basis for σ matrix as defined before. $|\uparrow_x\rangle_{\text{spin}}$ and $|\downarrow_x\rangle_{\text{spin}}$ indicate the spin up and down along x-direction. Thus, the expectation value of inter-orbital pairing is zero for these wavefunctions because the orbital states of the wavefunctions in Eqs. (76) and, (77) are same. On the other hand, when $n_1 \neq 0$, the x-component of the orbital pseudo-spin is generated (indicated in the large cyan arrows in Fig. 8d). The wave functions at $k_z = \pm k_s$ are given by

$$\left|\hat{\mathbf{d}}_+\right\rangle_{\text{orbital}} \otimes |\uparrow_x\rangle_{\text{spin}}, \quad \left|\hat{\mathbf{d}}_-\right\rangle_{\text{orbital}} \otimes |\downarrow_x\rangle_{\text{spin}}, \quad \text{for } k_z = +k_s, \tag{78}$$

$$\left|\hat{\mathbf{d}}_-\right\rangle_{\text{orbital}} \otimes |\uparrow_x\rangle_{\text{spin}}, \quad \left|\hat{\mathbf{d}}_+\right\rangle_{\text{orbital}} \otimes |\downarrow_x\rangle_{\text{spin}}, \quad \text{for } k_z = -k_s, \tag{79}$$

where $\mathbf{d}_\pm = (\pm n_1 \sin k_0, 0, -v_z(k_0 - k_s))$. Therefore, under the lattice distortion, the expectation value of the inter-orbital pairing is allowed and Δ_2 pairing is enhanced. This mechanism for the enhancement of unconventional pairings can be applied to the other cases. In summary, the emergence of unconventional superconductivity under lattice distortion can be understood due to the enhancement of inter-orbital pairings and DOS at Fermi surfaces.

Topological superconductivity of doped Dirac semimetal.

As summarized in Table 8, we characterize possible superconducting states in doped Dirac semimetal by the gap structures, topological winding numbers, and surface spectra.

First, the conventional superconducting phase having Δ_1 pairing potential can emerge. Because T_c of the Δ_1 phase increases under lattice distortions as shown in Figs. 5 and 6, conventional fully-gapped s-wave superconductivity can emerge.

Second, we consider the inversion-odd-parity superconductor. The BdG Hamiltonian in Eq. (23) are included in the DIII class according to 10-fold Altland-Zirnbauer classes[4,59] because $T^2 = -1$, $C^2 = +1$, and $\Gamma^2 = +1$. With the additional inversion symmetry, the DIII class superconductor can be an inversion-odd-parity topological superconductor[57] classified by Z_2 invariants $(-1)^{w_{\text{DIII}}}$, where

$$w_{\text{DIII}} = -\int \frac{d^3k}{48\pi^3} \varepsilon_{\mu\nu\rho} \text{Tr}[\Gamma(Q\partial_\mu Q)(Q\partial_\nu Q)(Q\partial_\rho Q)]. \tag{80}$$

Here, Γ is the chiral operator, and Q is the so-called Q-matrix[4,59] (or projection matrix). The sufficient condition for realizing the inversion-odd-parity topological superconductor is that it has an inversion-odd-parity pairing with a full gap and its Fermi surface encloses an odd number of time-reversal-invariant momenta. In the absence of lattice distortions, the inversion-odd-parity pairings, Δ_2, Δ_3, Δ_{41}, and Δ_{42}, are not fully gapped (Fig. 2a) and cannot be such a topological superconductor. However, under the lattice distortions, these inversion-odd-parity phases can be fully gapped, and the sufficient condition above can be satisfied for the large chemical potential ($\mu > M_0$) because the Fermi surface can enclose only (0, 0, 0) in BZ. However, when the chemical potential is large with a lattice distortion, the band structure near the Fermi energy is far from that of DSM. Because we are discussing the Dirac physics, we do not consider such a superconducting phase in this work.

Third, topological mirror superconducting phases[36,63] can exist under lattice distortions. Topological DSM has a nontrivial mirror Chern number defined in the M_{xy} plane and the corresponding surface states on the

mirror-symmetric boundary[36,39]. Similarly, topological mirror superconductivity for Δ_2 and Δ_3 phases can exist under lattice distortions. Under the n_1 (n_2) type lattice distortion, Δ_2 (Δ_3) phase is fully gapped, the Δ_2 (Δ_3) pairing potential is mirror-odd under the M_{xy} symmetry, and the mirror Chern number defined in M_{xy} plane is nontrivial ($C_M = \pm 2$), which leads to topological mirror superconductivity with a topologically-protected Majorana states on the mirror symmetric boundary. For example, see the gapless surface spectra of Δ_2 and Δ_3 phases in Region III in Fig. 4a, b, e, f. Due to the TRS and IS, this topological mirror superconductor is classified as $2\mathbb{Z}$.

Fourth, topological line nodal superconducting phases can exist under lattice distortions. As discussed in Fig. 3b, c, the inversion-even-parity Δ_1' pairing allows a topologically-protected nodal lines protected by the chiral winding number in Eq. (43). According to this chiral winding number, in general, the topological line nodal superconductor in doped topological DSM is classified as $2\mathbb{Z}$. The reason is as follows. Since there are PT and PC, the nodal points are fourfold degenerate, which means that there are even number of winding source at the same points. Therefore, our generic model has a topological winding number of even integers. Note that the topological class of a line node in 3D DIII superconductor using Clifford algebra[61] is $2\mathbb{Z}$, which is consistent with our result. However, there is no surface state because Δ_1' phase has two nodal lines having opposite chiral winding numbers (Fig. 3a).

Fourth, topological point nodal superconducting phases can exist under lattice distortions. For an inversion-odd-parity and mirror-even-parity pairing potential, we have a topological point nodal superconductor of which nodal points are protected by the mirror chiral winding number in Eq. (47). Because the chiral winding number is zero for inversion-odd-parity superconductor ($W = W_{\lambda=i} + W_{\lambda=-i} = 0$), the mirror chiral winding number is given by $W_M = W_{\lambda=i} - W_{\lambda=-i} = 2W_{\lambda=i}$. From this mirror chiral winding number, this topological point nodal superconductor is classified as $2\mathbb{Z}$. Note that the classification of a point node using Clifford algebra[4,61] is $M\mathbb{Z}$ considering one mirror sector, which is consistent with our results.

Discussion

Now, we compare our results with experimental works in doped DSM of Au_2Pb[30–34] and Cd_3As_2[27–29]. Au_2Pb shows superconductivity at $T_c \approx 1.2$K with D_{2h} symmetry at the ambient pressure[30,32,34]. This structural transition corresponds to the n_1 or n_2 type lattice distortion. T_c increases to 4 K until 5 GPa under compression[34]. The point-contact measurements also reported that $T_c \approx 2.1$ K using a hard contact tip is higher than the measured $T_c \approx 1.13$ K using a soft tip. Assuming that the hard tip induces higher pressure than the soft tip, the experimental results are consistent with our result that T_c is enhanced with increasing n_1 or n_2 lattice distortion (Fig. 5). The experiments reported that the superconductivity is either conventional[33,34] or unconventional[32] depending on the physical situations. From our analysis, the superconducting phase of Au_2Pb is expected to be either a conventional fully gapped or unconventional topological mirror superconductor with a gapless SABS depending on physical parameters.

Similarly, in Cd_3As_2, the structural phase transition occurs near 2.6 GPa, resulting in a monoclinic lattice C_{2h}. Then, a superconductivity emerges at $T_c \approx 1.8$ K under pressure higher than 8.5 GPa. This structural transition corresponds to n_3 or n_4 type lattice distortion. When the pressure increases further, T_c keeps increasing from 1.8 K (8.5 GPa) to 4.0K (21.3 GPa), which is consistent with the enhancement of T_c under lattice distortions (Fig. 6). In this case, n_1 or n_2 can also be added without breaking the symmetry further. From our analysis, the superconducting phases of Cd_3As_2 are expected to be either a conventional or topological mirror superconductor with a gapless SABS. We emphasize that the topological nodal superconductor having a flat SABS can appear only if either n_3 or n_4 lattice distortion is turned on. The point-contact measurements for Cd_3As_2 showed the zero-bias conductance peak (ZBCP) and double conductance peaks symmetric around zero bias, which was interpreted as a signal of a Majorana surface states[27–29]. Even though our result cannot directly explain the result of the point-contact measurement, the unconventional superconductivity having gapless Majorana fermion can emerge regardless of the lattice distortions according to the surface spectra (see Fig. 4), which seems to support the measured conductance peaks. Further experimental studies that reveal the nature of superconductivity are necessary, and our theoretical results will be a helpful guideline to interpret the experimental result and search for the possible topological superconductivity in DSM.

The other way to induce superconductivity in DSM is to use the proximity effect. Recently, an 1D proximity-effect-induced superconductivity in Cd_2As_3 Dirac semimetal nanowire-based Josephson junctions is reported, where the superconductivity is induced by the proximity effect from conventional s-wave superconductor[64,65]. On the other hand, the lattice-distortion-induced superconductivity in this work is intrinsic and three-dimensional. Interestingly, a strain-induced topological superconductivity with Majorana bound states was also reported in 2D Dirac semimetals[66]. We expect that combining these approaches would be helpful to generate and manipulate Majorana bound states, which is compatibly applicable to future quantum information technologies.

Summary

In this work, we have studied the possible symmetry-lowering lattice distortions and their effects on the emergence of unconventional superconductivity in doped topological DSM. From the group theoretical analysis, four types of symmetry-lowering lattice distortions that reproduce the crystal systems present in experiments are identified. We investigated the possible superconductivity under such symmetry-lowering lattice distortions considering inter-orbital and intra-orbital electron density-density interactions. We found that both conventional and unconventional superconductivity can emerge depending on the lattice distortion and electron density-density interaction. Remarkably, the unconventional inversion-odd-parity superconductivity hosts gapless surface Andreev bound states (SABS) even under lattice distortions. We found that the lattice distortion enhances the superconducting critical temperature. Therefore, our work is consistent with the observed structural phase transition and the enhancement of superconductivity in Cd_3As_2 and Au_2Pb under pressure. We also suggest that

enhanced conventional and unconventional superconductivity in doped topological DSM can be controlled by physical parameters such as the pressure and strength of the superconducting pairing interaction. Thus, our work will provide a valuable tool to explore and control the superconductivity in topological materials.

Methods

To study the effects of symmetry-lowering lattice distortions, we assume a minimal 4×4 Hamiltonian that describes representative topological Dirac semimetals[39,45], where the lattice distortions are implemented as a perturbation[53]. To study the superconductivity, we construct the Bogoliubov-de Gennes (BdG) Hamiltonian within the mean-field approximation while keeping TRS and the crystal symmetry[55,56]. The momentum independent pairing potentials are classified using irreducible representations of the unbroken point group[36,37,56–58]. The nodal structures, chiral winding number in Eq. (43), and chiral mirror winding number in Eq. (47) are calculated using the BdG Hamiltonian. The surface Green's functions are calculated using a Möbius transformation-based method[62]. The superconducting critical temperature T_c is calculated by solving the linearized gap equation in the weak-coupling limit[37,55–58]. All the details are provided in the main text and Supplementary Information.

Received: 12 July 2021; Accepted: 23 August 2021
Published online: 17 September 2021

References

1. Hasan, M. Z. & Kane, C. L. Colloquium: Topological insulators. *Rev. Mod. Phys.* **82**, 3045 (2010).
2. Qi, X.-L. & Zhang, S.-C. Topological insulators and superconductors. *Rev. Mod. Phys.* **83**, 1057 (2011).
3. Franz, M. & Molenkamp, L. *Topological Insulators* (Elsevier, 2013).
4. Chiu, C.-K., Teo, J. C., Schnyder, A. P. & Ryu, S. Classification of topological quantum matter with symmetries. *Rev. Mod. Phys.* **88**, 035005 (2016).
5. Ando, Y. & Fu, L. Topological crystalline insulators and topological superconductors: From concepts to materials. *Annu. Rev. Condens. Matter Phys.* **6**, 361–381 (2015).
6. Armitage, N., Mele, E. & Vishwanath, A. Weyl and dirac semimetals in three-dimensional solids. *Rev. Mod. Phys.* **90**, 015001 (2018).
7. Sato, M. & Ando, Y. Topological superconductors: A review. *Rep. Progr. Phys.* **80**, 076501 (2017).
8. Wan, X., Turner, A. M., Vishwanath, A. & Savrasov, S. Y. Topological semimetal and fermi-arc surface states in the electronic structure of pyrochlore iridates. *Phys. Rev. B* **83**, 205101 (2011).
9. Burkov, A., Hook, M. & Balents, L. Topological nodal semimetals. *Phys. Rev. B* **84**, 235126 (2011).
10. Young, S. M. *et al.* Dirac semimetal in three dimensions. *Phys. Rev. Lett.* **108**, 140405 (2012).
11. Hasan, M. Z. *et al.* Weyl, dirac and high-fold chiral fermions in topological quantum matter. *Nat. Rev. Mater.* **2021**, 1–20 (2021).
12. Nielsen, H. B. & Ninomiya, M. The adler-bell-jackiw anomaly and weyl fermions in a crystal. *Phys. Lett. B* **130**, 389–396 (1983).
13. Murakami, S. & Kuga, S.-I. Universal phase diagrams for the quantum spin hall systems. *Phys. Rev. B* **78**, 165313 (2008).
14. Yang, K.-Y., Lu, Y.-M. & Ran, Y. Quantum hall effects in a weyl semimetal: Possible application in pyrochlore iridates. *Phys. Rev. B* **84**, 075129 (2011).
15. Son, D. & Spivak, B. Chiral anomaly and classical negative magnetoresistance of weyl metals. *Phys. Rev. B* **88**, 104412 (2013).
16. Kim, H.-J. *et al.* Dirac versus weyl fermions in topological insulators: Adler-bell-jackiw anomaly in transport phenomena. *Phys. Rev. Lett.* **111**, 246603 (2013).
17. Hosur, P. & Qi, X. Recent developments in transport phenomena in weyl semimetals. *Comptes Rendus Physique* **14**, 857–870 (2013).
18. Vafek, O. & Vishwanath, A. Dirac fermions in solids: from high-T_c cuprates and graphene to topological insulators and Weyl semimetals. *Annu. Rev. Condens. Matter. Phys.* **5**, 83–112 (2014).
19. Okugawa, R. & Murakami, S. Dispersion of fermi arcs in weyl semimetals and their evolutions to dirac cones. *Phys. Rev. B* **89**, 235315 (2014).
20. Liang, T. *et al.* Ultrahigh mobility and giant magnetoresistance in the dirac semimetal Cd_3As_2. *Nat. Mater.* **14**, 280–284 (2015).
21. Yang, L. *et al.* Weyl semimetal phase in the non-centrosymmetric compound TaAs. *Nat. Phys.* **11**, 728–732 (2015).
22. Lv, B. *et al.* Experimental discovery of weyl semimetal TaAs. *Phys. Rev. X* **5**, 031013 (2015).
23. Burkov, A. A. & Kim, Y. B. Z_2 and chiral anomalies in topological dirac semimetals. *Phys. Rev. Lett.* **117**, 136602 (2016).
24. Yan, B. & Felser, C. Topological materials: Weyl semimetals. *Ann. Rev. Condensed Matter Phys.* **8**, 337–354 (2017).
25. Wang, S., Lin, B.-C., Wang, A.-Q., Yu, D.-P. & Liao, Z.-M. Quantum transport in dirac and weyl semimetals: A review. *Adv. Phys. X* **2**, 518–544 (2017).
26. Nagaosa, N., Morimoto, T. & Tokura, Y. Transport, magnetic and optical properties of weyl materials. *Nat. Rev. Mater.* **5**, 621–636 (2020).
27. Aggarwal, L. *et al.* Unconventional superconductivity at mesoscopic point contacts on the 3D Dirac semimetal Cd_3As_2. *Nat. Mater.* **15**, 32–37 (2016).
28. He, L. *et al.* Pressure-induced superconductivity in the three-dimensional topological dirac semimetal Cd_3As_2. *NPJ Quantum Matet.* **1**, 1–5 (2016).
29. Wang, H. *et al.* Observation of superconductivity induced by a point contact on 3D Dirac semimetal Cd_3As_2 crystals. *Nat. Mater.* **15**, 38–42 (2016).
30. Schoop, L. M. *et al.* Dirac metal to topological metal transition at a structural phase change in Au_2Pb and prediction of Z_2 topology for the superconductor. *Phys. Rev. B* **91**, 214517 (2015).
31. Chen, K. W. *et al.* Temperature-pressure phase diagram of cubic Laves phase Au_2Pb. *Phys. Rev. B* **93**, 045118 (2016).
32. Xing, Y. *et al.* Superconductivity in topologically nontrivial material Au_2Pb. *NPJ Quantum Mater.* **1**, 1–8 (2016).
33. Yu, Y. *et al.* Fully gapped superconducting state in Au_2Pb: A natural candidate for topological superconductor. *Europhys. Lett.* **116**, 67002 (2017).
34. Wu, J. *et al.* Ground states of Au_2Pb and pressure-enhanced superconductivity. *Phys. Rev. B* **100**, 060103 (2019).
35. Yu, W. *et al.* Zero-bias conductance peak in dirac semimetal-superconductor devices. *Phys. Rev. Res.* **2**, 032002 (2020).
36. Kobayashi, S. & Sato, M. Topological superconductivity in dirac semimetals. *Phys. Rev. Lett.* **115**, 187001 (2015).
37. Hashimoto, T., Kobayashi, S., Tanaka, Y. & Sato, M. Superconductivity in doped dirac semimetals. *Phys. Rev. B* **94**, 014510 (2016).
38. Murakami, S. Phase transition between the quantum spin hall and insulator phases in 3d: Emergence of a topological gapless phase. *New J. Phys.* **9**, 356 (2007).
39. Yang, B.-J. & Nagaosa, N. Classification of stable three-dimensional dirac semimetals with nontrivial topology. *Nat. Commun.* **5**, 1–10 (2014).
40. Gao, Z., Hua, M., Zhang, H. & Zhang, X. Classification of stable dirac and weyl semimetals with reflection and rotational symmetry. *Phys. Rev. B* **93**, 205109 (2016).

41. Steinberg, J. A. *et al.* Bulk dirac points in distorted spinels. *Phys. Rev. Lett.* **112**, 036403 (2014).
42. Liu, Z. *et al.* Discovery of a three-dimensional topological dirac semimetal, Na_3Bi. *Science* **343**, 864–867 (2014).
43. Xu, S.-Y. *et al.* Observation of fermi arc surface states in a topological metal. *Science* **347**, 294–298 (2015).
44. Wang, Z. *et al.* Dirac semimetal and topological phase transitions in A_3Bi (A=Na, K, Rb). *Phys. Rev. B* **85**, 195320 (2012).
45. Wang, Z., Weng, H., Wu, Q., Dai, X. & Fang, Z. Three-dimensional dirac semimetal and quantum transport in Cd_3As_2. *Phys. Rev. B* **88**, 125427 (2013).
46. Neupane, M. *et al.* Observation of a three-dimensional topological dirac semimetal phase in high-mobility Cd_3As_2. *Nat. Commun.* **5**, 1–8 (2014).
47. Jeon, S. *et al.* Landau quantization and quasiparticle interference in the three-dimensional dirac semimetal Cd_3As_2. *Nat. Mater.* **13**, 851–856 (2014).
48. Liu, Z. *et al.* A stable three-dimensional topological dirac semimetal Cd_3As_2. *Nat. Mater.* **13**, 677–681 (2014).
49. Borisenko, S. *et al.* Experimental realization of a three-dimensional dirac semimetal. *Phys. Rev. Lett.* **113**, 027603 (2014).
50. Chen, K. *et al.* Temperature-pressure phase diagram of cubic laves phase Au_2Pb. *Phys. Rev. B* **93**, 045118 (2016).
51. Chen, R. *et al.* Optical spectroscopy study of the three-dimensional dirac semimetal $ZrTe_5$. *Phys. Rev. B* **92**, 075107 (2015).
52. Li, Q. *et al.* Chiral magnetic effect in $ZrTe_5$. *Nat. Phys.* **12**, 550–554 (2016).
53. Stoneham, A. M. *Theory of Defects in Solids: Electronic Structure of Defects in Insulators and Semiconductors* (Oxford University Press, 2001).
54. Fu, L., Kane, C. L. & Mele, E. J. Topological insulators in three dimensions. *Phys. Rev. Lett.* **98**, 106803 (2007).
55. Alexandrov, A. S. *Theory of Superconductivity: From Weak to Strong Coupling* (CRC Press, 2003).
56. Bennemann, K.-H. & Ketterson, J. B. *Superconductivity: Volume 1: Conventional and Unconventional Superconductors Volume 2: Novel Superconductors* (Springer Science & Business Media, 2008).
57. Fu, L. & Berg, E. Odd-parity topological superconductors: Theory and application to $Cu_xBi_2Se_3$. *Phys. Rev. Lett.* **105**, 097001 (2010).
58. Nakosai, S., Tanaka, Y. & Nagaosa, N. Topological superconductivity in bilayer rashba system. *Phys. Rev. Lett.* **108**, 147003 (2012).
59. Schnyder, A. P., Ryu, S., Furusaki, A. & Ludwig, A. W. Classification of topological insulators and superconductors in three spatial dimensions. *Phys. Rev. B* **78**, 195125 (2008).
60. Koshino, M., Morimoto, T. & Sato, M. Topological zero modes and dirac points protected by spatial symmetry and chiral symmetry. *Phys. Rev. B* **90**, 115207 (2014).
61. Kobayashi, S., Shiozaki, K., Tanaka, Y. & Sato, M. Topological blount's theorem of odd-parity superconductors. *Phys. Rev. B* **90**, 024516 (2014).
62. Umerski, A. Closed-form solutions to surface green's functions. *Phys. Rev. B* **55**, 5266 (1997).
63. Zhang, F., Kane, C. & Mele, E. Topological mirror superconductivity. *Phys. Rev. Lett.* **111**, 056403 (2013).
64. Wang, A.-Q. *et al.* 4π-periodic supercurrent from surface states in Cd_3As_2 nanowire-based josephson junctions. *Phys. Rev. Lett.* **121**, 237701 (2018).
65. Li, C.-Z. *et al.* Topological transition of superconductivity in dirac semimetal nanowire josephson junctions. *Phys. Rev. Lett.* **126**, 027001 (2021).
66. Alidoust, M., Willatzen, M. & Jauho, A.-P. Strain-engineered majorana zero energy modes and φ_0 josephson state in black phosphorus. *Phys. Rev. B* **98**, 085414 (2018).

Acknowledgements

This work was supported by National Research Foundation (NRF) of Korea Grant funded by the Korea government (MSIT) (Nos. 2018R1C1B6007607, 2021R1H1A1013517, 2021R1C1C1008738, 2020R1A2C1007554, 2021R1A2C4002773, and 2021R1A5A1032996). S.C. was also supporte by the research fund of the POSCO Science Fellowship of POSCO TJ Park Foundation. S.B.C. was also supported by the National Research Foundation (NRF) of Korea grants funded by the Ministry of Education (2018R1A6A1A06024977). B.-J.Y. was also supported by the Institute for Basic Science in Korea (Grant No. IBS-R009-D1), Samsung Science and Technology Foundation under Project No. SSTF-BA2002-06, the U.S. Army Research Office and Asian Office of Aerospace Research & Development (AOARD) under Grant No. W911NF-18-1-0137.

Author contributions

B.-J.Y. conceived the project. S.C. and K.H.L. performed the theoretical and numerical calculations. All authors analyzed the results. S.C. and K.H.L. wrote the manuscript. All authors reviewed the manuscript.

Competing interests

The authors declare no competing interests.

Additional information

Supplementary Information The online version contains supplementary material available at (https://doi.org/10.1038/s41598-021-97982-1).

Correspondence and requests for materials should be addressed to S.B.C. or B.-J.Y.

Reprints and permissions information is available at www.nature.com/reprints.

Publisher's note Springer Nature remains neutral with regard to jurisdictional claims in published maps and institutional affiliations.